UNIVERSITÀ DEGLI STUDI DI PADOVA

Dipartimento di Fisica e Astronomia "Galieo Galiei"

Master Degree in Astrophysics and Cosmology

Final Dissertation

Characterization of the extreme blazar PG 1553+113 with the early data from the Large-Sized Telescope (LST-1) of the Cherenkov Telescope Array (CTA)

Thesis Supervisor:
Prof. Mosè Mariotti
Thesis Co-Supervisor:
Dr. Davide Miceli

Candidate:
Helena Luciani

Academic year 2022/2023

To my grandfather and my daughter,
to what has been and what will be.

Contents

Abstract

In the Very-High Energy (VHE) γ-ray domain (E > 100 GeV) non-thermal phenomena can be investigated, which occur in galactic sources as Supernova Remnants (SNRs) and Pulsars (PSRs), and extragalactic ones, like Active Galactic Nuclei (AGNs) and Gamma-Ray Bursts (GRBs). The detection of this emission requires indirect methods, and the most accredited one involves making use of the Cherenkov emission produced within extensive air showers resulting from the interaction of VHE γ-rays with the atmosphere.

AGNs are strong VHE γ-ray emitters, due to the accretion activity of the supermassive black hole (SMBH) that powers these compact regions located at the center of host galaxies. A limited fraction of AGNs ($\sim$10%) exhibit jets, two narrow beams along the rotation axis of the black hole from which are ejected relativistic particles, predominantly electrons and positrons. Among jetted AGNs there are blazars, a class of objects characterized by the fact that the jet is oriented along the line of sight of the observer. They are distinguished by strong and variable polarized emission. Blazars are classified into two subclasses, based on the presence of emission lines in their spectra. Flat-Spectrum Radio Quasars (FSRQs) have prominent broad emission lines in their spectra, while BL Lacertae (BL Lacs) objects exhibit weak or no emission lines and their entire emission is defined by the jet.

PG 1553+113 is a BL Lac object, located at redshift z=0.433, that has been long studied and monitored during the years across almost the entire electromagnetic spectrum. Numerous multi-band campaigns have been conducted on PG 1553+113, from which it has been inferred that the most suitable model to describe its emission is a single-zone SSC model. PG 1553+113 is among the few blazars whose flux variability is claimed to be periodic in some bands, but not really confirmed in others bands. *Fermi-LAT* performed a continuous monitoring on PG 1553+113, revealing a quasi-periodic emission in the high-energy γ-ray band of 2.18 $\pm$ 0.08 years. Moreover, an intra-day variability of 2.4 $\pm$ 0.7 kiloseconds (corresponding to approximately 0.67 hours) was recently found in the X-ray energy range from data collected by *XMM-Newton*. The features in the high-energy γ-ray light curve of PG 1553+113 make it one of the few candidates of a binary system of two SMBHs.

The aim of this thesis is to characterize the extreme blazar PG 1553+113 in the VHE regime, exclusively using early data from the Large-Sized Telescope (LST-1), part of the Cherenkov Telescope Array (CTA). Periodic behaviour or short-time variability has not been observed yet in the VHE band, and one of the objectives of the thesis is to search for an hint of intra-night

variability of the source. The identification of rapid fluctuations will provide an important tool for constraining the emission model and determining the size of the emitting region.

The entire dataset ranges from March 2021 to April 2023. In the first part of this thesis, the LST-1 data analysis of the two years dataset is presented. It covers an observation time of 24.84 hours. A strong evidence of the detection of a γ-ray signal from the blazar has been found. Both observed and intrinsic spectrum are presented, considering the decrease in flux resulting from the interaction with the Extragalactic Background Light (EBL). Run-wise and night-wise binned light curves are produced to perform a long-term monitoring of the blazar.

The second part of this work is dedicated to the analysis of the flare observed on the night of April 25th 2023, during which a deep observation of PG 1553+113 lasting 4 hours was required. The reason is the desire to investigate a possible intra-night variability of the source and verify the presence of a correlation with the X-ray band. This observation was done by taking advantage of the high-state of emission predicted for the current year from the Fermi periodicity. Light curve, differential spectrum, spectral energy distribution and other valuable insights are extracted from data. The light curve is binned in short-time intervals of the order of minutes to search for rapid flux variations.

A χ^2 statistical test is performed after the light curves have been fitted with a constant flux, to test how much the emission of the source deviates from a steady behaviour. This test is applied to both light curves, the two-year one and the single-night one. From the two-year dataset, it is obtained $\chi^2_{red} \approx 5.78$, indicating that a constant flux does not appropriately describe the emission of the source, as expected for a blazar. From the single-night dataset results $\chi^2_{red} \approx 2.85$, suggesting an hint of intra-night variability.

Chapter 1

Active Galactic Nuclei

Active Galactic Nuclei (AGNs) are massive compact objets located at the center of galaxies. They are strong emitters, powered by an **actively accreting supermassive black hole (SMBH)**, with a typical mass $\geq 10^6 \mathrm{M}_\odot$ [1]. AGNs have many properties, which include [1]:

- very high luminosities, up to $L_{bol} \sim 10^{48}$ erg s^{-1};
- variable emission, with typical timescales ranging from hours to years, due to changes in the accretion rate, interactions between disk and SMBH and variations of magnetic field;
- small emitting regions in most bands, with a size related to the variability timescale;
- strong evolution of the luminosity function;
- detectable emission covering all the electromagnetic spectrum.

The schematic structure of an AGN is shown in Figure 1.1. The central SMBH is surrounded by an **accretion disk**, in which dissipative processes transport matter inwards and angular momentum outwards, heating up the disk to extremely high temperatures (T > 10^4 K). Around the disk, a thick structure of gas and dust forms the **obscuring torus**. Other relevant regions are: the **broad-line region (BLR)** and the **narrow-line region (NLR)**, responsible for the emission lines observed in AGNs spectra. They are formed by heavy ionized clouds, in which the gas moves at velocities that range from ∼100 km/s (NLR) to ∼1000-10000 km/s in the BLR. Some AGNs present two **jets** emerging from the center.
Each individual component contributes to a **distinct emission** within the spectrum, as seen in Figure 1.2. The infrared (IR) band is mostly sensitive to obscuring material from the torus and dust, the optical/ultraviolet (UV) band is related to emission from the accretion disk, while the X-ray traces the emission of the hot plasma around the disk. γ-ray and radio bands are characterized by strong non-thermal emission associated to the jet.

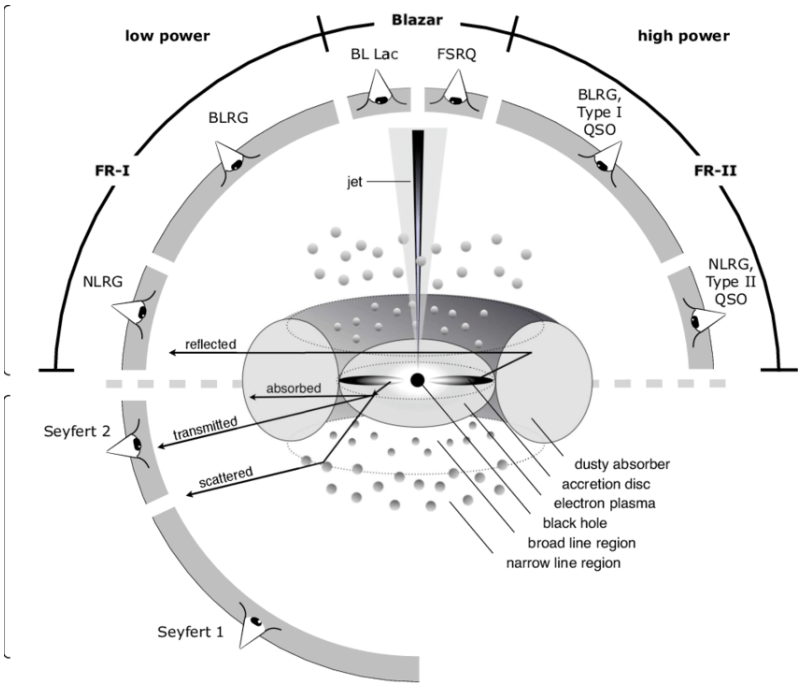

Figure 1.1: Schematic representation of an AGN. The type of object seen depends on the spectral features, consequence of the observing angle [2].

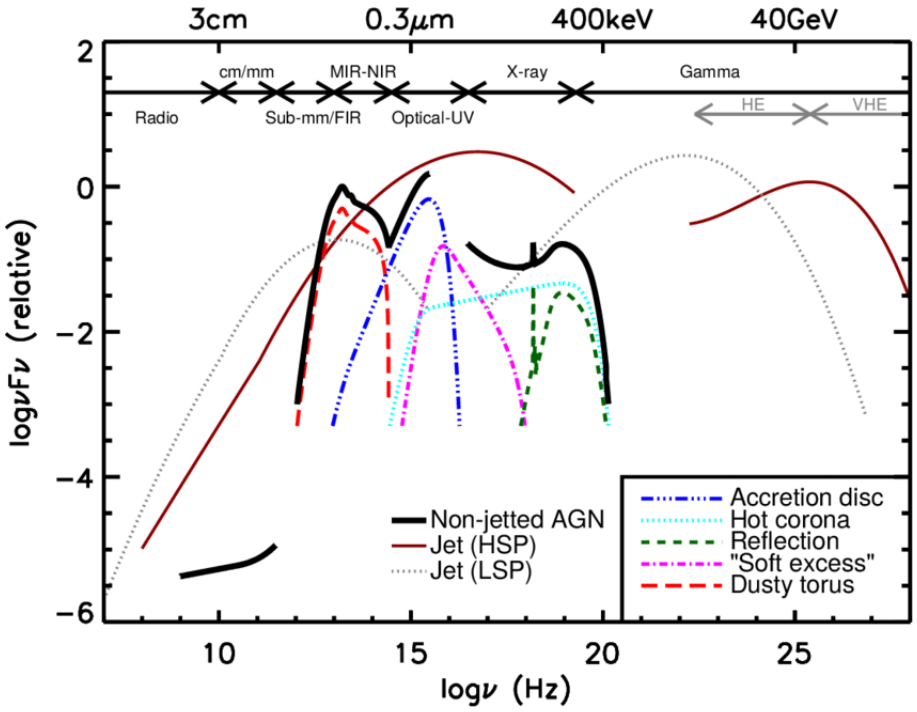

Figure 1.2: The spectral energy distribution (SED) of an AGN. The black solid curve represents the total emission of a non-jetted AGN, and the various coloured curves (shifted down for clarity) represent the individual components [1].

AGNs can be classified into distinct categories based on their **spectral features**, resulting in a large number of different types at which the literature commonly refers as *AGN "zoo"*. The observed type depends on the viewing angle between the observer and the object (see Fig. 1.1), which is crucial in shaping its spectral properties. AGNs are classified in two main classes, based on the relevance of the radio emission:

- **Radio-quiet AGNs**: Seyfert Galaxies, Quasars. The multi-band emission is dominated by thermal processes, and radio emission can be related to star formation.
- **Radio-loud AGNs**: Radio Galaxies, Blazars, Radio-loud Quasars. The emission is dominated by non-thermal processes related to the jet. Only a limited fraction of AGNs ($\sim$10%) has jets.

1.1 Blazars

Blazars are a class of AGNs characterized by **rapid spectral variability**, assumed to be due to the presence of a **relativistic jet** pointing very close to the line of sight. The jet is generated by the strong acceleration and the intense magnetic field that particles experience during the accretion. Attracted by the strong gravity, matter falls towards the central black hole, but a small fraction of particles get accelerated to relativistic speeds and ejected in two narrow beams along the rotation axis of the black hole. The jet is formed by highly energetic charged particles, predominantly electrons and positrons, producing a **non-thermal emission** across the entire electromagnetic spectrum, from radio to γ-rays.

Blazars are classified into two subclasses, based on their spectral features: **Flat-Spectrum Radio Quasars (FSRQs)** and **BL Lacertae (BL Lacs)** objects (see Fig. 1.3).
FSRQs have **prominent broad emission lines** in their spectra, indicating a powerful accretion disk and dense surrounding gas. Its emission is interpreted as the superposition of the jet emission, the IR torus and the hot corona.
BL Lacs, on the other hand, exhibit **weak or no emission lines**, suggesting lower accretion rates and less surrounding gas. The entire emission is defined by the radiation from the jet, with a contribution from the host galaxy in the sub-optical spectral range. Both subclasses exhibit **strong and variable polarized emission**, which is a characteristic feature of these objects. Generally, BL Lac objects are located at smaller z, mostly below z $\sim$ 1, exhibiting lower average luminosity (10^{43}- 10^{45} erg s^{-1}). Instead, FSRQs are located at intermediate and large z, with a larger average luminosity (> 10^{45} erg s^{-1}) [3].

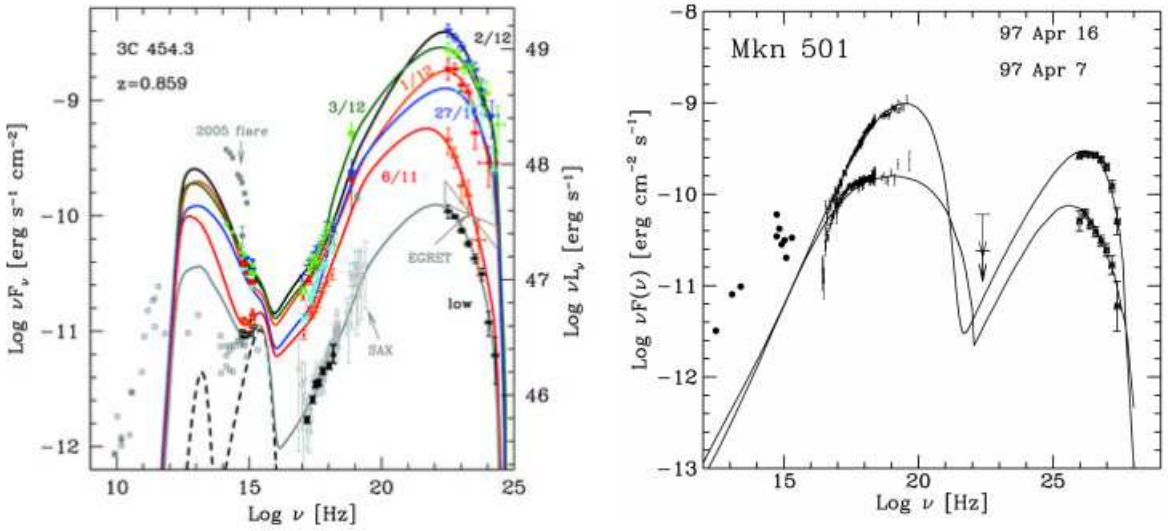

Figure 1.3: Examples of spectral energy distributions (SEDs) of a FSRQ (*left*, 3C 454.3) and a BL Lac object (*right*, Mkn 501). In the SED of 3C 454.3, in addition to the jet emission, it can be identified an accretion disk component, the X-ray corona contribution and the IR emission from the torus (dashed black lines). In Mkn 501, instead, only the contributions from the jet and host galaxy are evident [3].

The blazar **variability** is generally divided into the following three classes, according to the observed variability timescale [4]:

- Long Term Variability (LTV): ranges from months to several years or decades;
- Short Term Variability (STV): between few days to weeks or months;
- Intra Day/Night Variability (IDV): from minutes to hours or less than one day.

The long term variability in the emission is likely associated with variations in the accretion rates onto the SMBH. On the other hand, the short term variability is generally attributed to the propagation of shocks inside the jet. The rapid variability observed on intra-day/night timescales is typically seen in X-ray and γ-ray light curves, and implies that fluctuations in flux arise within the jet. The more likely mechanisms occuring in the jet are magnetic irregularities or changes in the viewing angle of the discrete emission regions [4].
The timescales of variability and the related parameters can be used to probe the intrinsic emission properties, such as radiative mechanisms, dimensions and position of the emission region within the jet, and the mass of the supermassive black hole.

1.1.1 Emission models

The emission of blazars is **non-thermal** over most of the electromagnetic spectrum. The observed spectral energy distribution (SED) of a blazar has a typical shape composed of **two**

broad humps. The first one typically peaks between the far-infrared and the soft X-ray band, due to **synchrotron emission** produced by high-energy electrons spiraling in the magnetic field. The second peak, typically in the hard X-ray to γ-ray bands, is due to **Inverse Compton (IC) scattering**, where high-energy electrons interact with photons to boost them to γ-ray energies [3].

When the high-energy electrons, responsible for emitting synchrotron radiation, interact through inverse Compton with photons previously generated in their surroundings, the corresponding model is referred to as **Synchrotron Self-Compton (SSC)** [3]. The SSC model is the most widely accepted model for explaining the emission of blazars, and it is schematically explained in Figure 1.4.

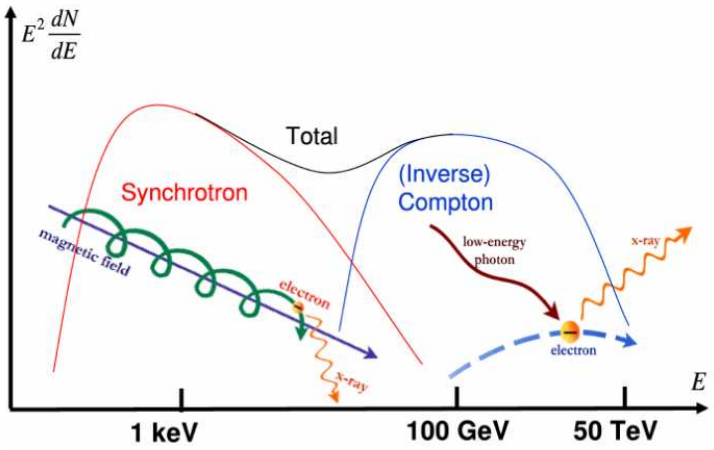

Figure 1.4: Differential energy spectrum of photons in the SSC model [5].

Further sub-divisions depending on the **location of the peak of the synchrotron component** are applied on BL Lacs objects. They result to be divided into:

- low-energy peaked BL Lacs (LBL),
- high-energy peaked BL Lacs (HBL),

whether the peak of the synchrotron emission lies in the IR–optical or UV–soft-X band, respectively (see Fig. 1.5). FSRQs instead are characterized by synchrotron peaks mainly at IR–optical frequencies, similarly to LBLs (see Fig. 1.5).

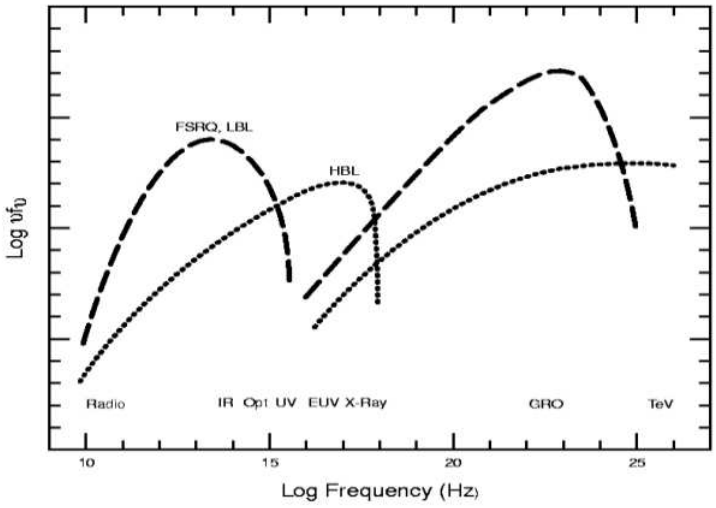

Figure 1.5: Spectral energy distributions of HBL, LBL and FSRQ objects. Both peaks are represented, with an emphasis on the synchrotron peak, which is indicated by the location of the object names.

The orientation of blazar's jet results in strong **relativistic Doppler beaming**, which enhances the emission. This relativistic effect makes the jet emission appear much brighter and more luminous, producing the intense radiation observed across the entire electromagnetic spectrum. The luminosity is enhanced by a factor δ^p:

$$L_{obs} = \delta^p L_{em} \tag{1.1}$$

where $\delta = \frac{1}{\gamma(1-\beta\cos\theta)}$ is the Doppler boosting factor and p depends on the emitted spectrum shape and the jet physics: $p = 3 + \alpha$ is for a moving compact source and $p = 2 + \alpha$ for a continuous jet (α is the spectral index) [6].

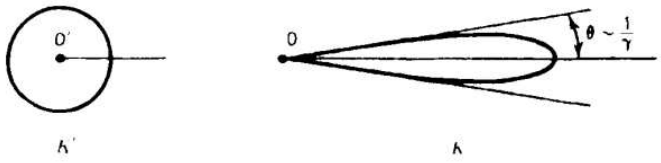

Figure 1.6: Relativistic beaming of radiation emitted isotropically.

1.1.2 The blazar sequence

The blazar sequence connects the observed **bolometric luminosity** (the total power emitted across all radiation frequencies) to the shape of the spectral energy distribution. Blazars with **greater bolometric luminosity** have 'redder' SEDs, associated to LBLs, and their high-energy peak is more prominent. Blazars with **lower bolometric luminosity** have instead a

'blue' SED, and are associated to HBLs, with the two peaks having approximately the same luminosity [7].

The primary hypothesis proposed by Fossati et al. [8] suggests that the spectral energy distribution can exhibit changes as luminosity increases. Specifically, with increasing luminosity both the synchrotron peak and the inverse Compton peak **move to lower frequencies** and the Compton component becomes energetically more dominant. Moreover, they predicted that TeV emitters have relatively low intrinsic luminosity.

In Figure 1.7 are shown the **'original' phenomenological sequence** and the **'updated' one**, obtained by Donato et al. [9]. The difference between the two sequences lies in the fact that in the latest sample are added the 2–10 keV (X-rays) average spectral indices and fluxes. The larger dataset aims to unify the different behaviors of blazars by utilizing a single parameter: the observed bolometric luminosity.

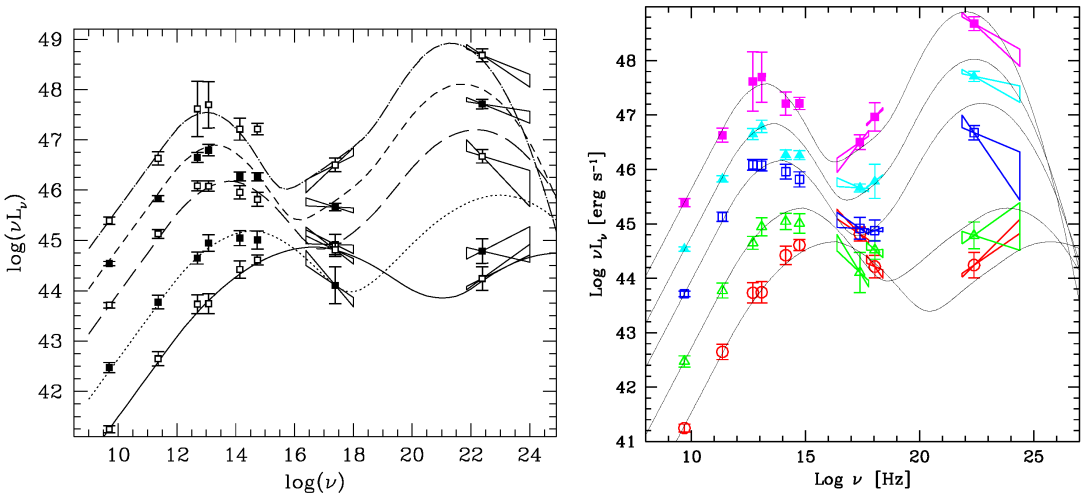

Figure 1.7: *Left*: The original blazar sequence. *Right*: The updated sequence [3].

A **theoretical interpretation** of the sequence relates the γ-peak to the amount of radiative cooling. The spectral sequence was interpreted by Ghisellini et al. [10] as due to the larger radiative cooling experienced by the electrons emitting in more powerful blazars. In these cases, the radiation energy density is significantly influenced by photons originating outside the jet. A stronger cooling results in a break at lower energies of the energy distribution, and in an increased output of energy through the inverse Compton process, leading to the prevalence of the high-energy peak.

A revised sequence was proposed after the observations by the *Fermi-LAT* satellite of about 1500 blazars (as reported in the 3LAC catalog) in the γ-ray band, and it was named **Fermi**

blazar sequence. The sequence was developed on a sample of γ-ray selected blazars, exhibiting a more complex scenario with respect to the original one, in part explained by the presence of blazars with a wide range of black hole masses. One of the main differences with respect to the previous sequence lies on the considered parameters. The 'original' blazar sequence is based just on the bolometric luminosity parameter, while the Fermi sequence takes into account many other parameters, such as the three typical frequencies of the spectrum (the self-absorption ν_t, the frequency of the synchrotron peak ν_s, the frequency of the Compton peak ν_c) and the two $\nu L(\nu)$ luminosities at the synchrotron and Compton peaks. The Fermi blazar sequence is shown in Figure 1.8.

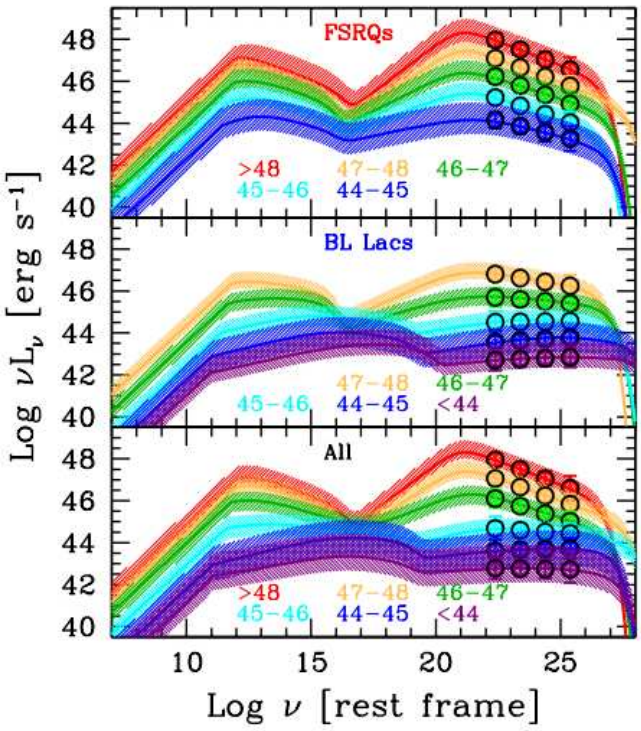

Figure 1.8: The Fermi blazar sequence. (*Top*) FSRQs objects of different luminosity, showing an increase in Compton component for increasing luminosity. (*Middle*) BL Lacs objects: both the synchrotron and the Compton peak frequencies become smaller increasing the bolometric luminosities. (*Bottom*) FSRQs and BL Lacs merged together. A clearer sequence can be seen [11].

1.2 Gamma-ray attenuation

Extragalactic sources are affected by the so called **gamma-ray attenuation**, due to the interaction of very-high energy γ-rays with **diffuse low energy photons**, such as the Cosmic Microwave Background (CMB) and Extragalactic Backgound Light (EBL). This interaction

produces e^+e^- pairs, leading to an **attenuation of the very high-energy** part of the spectrum.

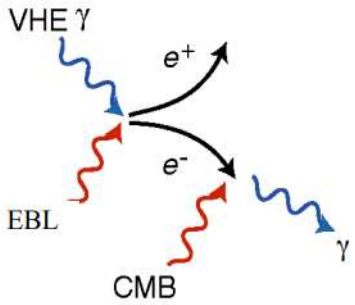

Figure 1.9: Schematic representation of the interaction between very-high energy γ-ray and Extragalactic Background Light (EBL).

The probability for this process to happen depends on the cross section for pair production, which increases at increasing energy, and on the distance that very-high energy photons have to propagate through. The gamma-ray attenuation is calculated by integrating the cross section times the proper density of background photons along the line of sight to the emitting redshift, and integrating over the scattering angle [12].

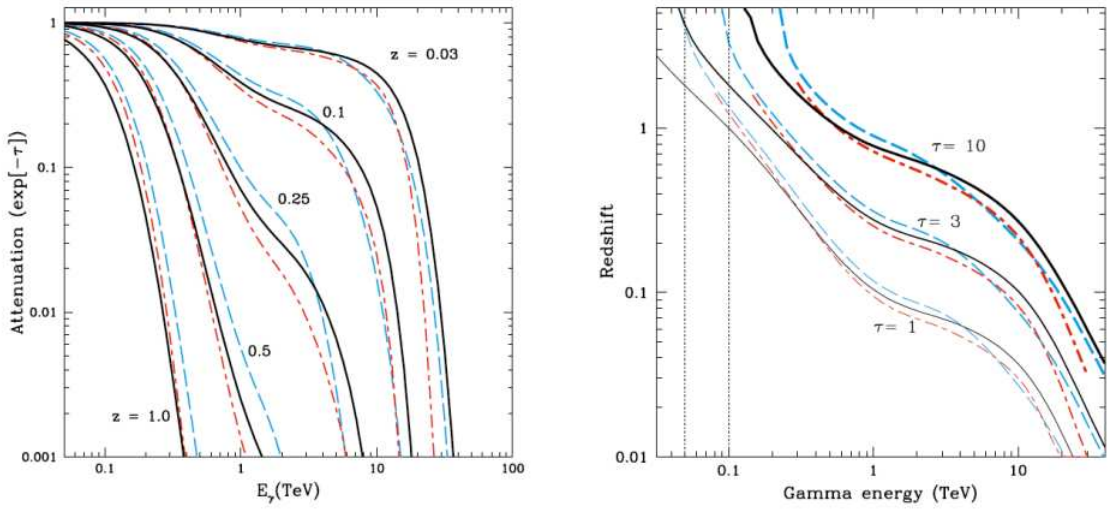

Figure 1.10: (*Left Panel*) Gamma-ray attenuation for photons of observed energy E_γ from sources at redshifts 0.03, 0.1, 0.25, 0.5, and 1. (*Right Panel*) The curves show the redshift at which the pair-production optical depth $\tau(E, z)$ reaches the value 1, 3, or 10 as a function of observed γ-ray energy [12].

In Figure 1.10 are presented two relations that explain the gamma-ray attenuation. One represents the attenuation as a function of the redshift of the source and the observed γ-ray

energy (*left panel*). The other one (*right panel*) represents the evolution of the optical depth τ as a function of the redshift and γ-ray energy. According to these considerations, it is possible to affirm that the gamma-ray attenuation is negligible for galactic photons, but it is relevant for extragalactic ones.

This effect affects the spectrum of the source, resulting in a decreasing flux at very-high energies (E $\geq$ TeV). As a consequence, very-high energy spectra of extragalactic sources show **high-energy exponential cutoffs** $\propto e^{-\tau(E,z)}$, where $\tau(E,z)$ is the pair-production optical depth, that is in function of the γ-ray energy and the redshift of the source. For this reason, the observed spectrum S_{obs} has to be corrected for this quantity to obtain the intrinsic spectrum S_{int} (see the example in Figure 1.11) [13]:

$$S_{obs} = S_{int} \cdot e^{-\tau(E,z)} \tag{1.2}$$

The absorption is maximum when the product of the two photon energies ϵ equals on average the square of the rest-mass energy [13]:

$$\epsilon_{max} \approx \frac{2(m_e c^2)^2}{E_\gamma} \approx 0.5 \left(\frac{1TeV}{E_\gamma}\right) \tag{1.3}$$

in which $(m_e c^2)$ is the rest-mass energy and E_γ is the γ-ray energy.

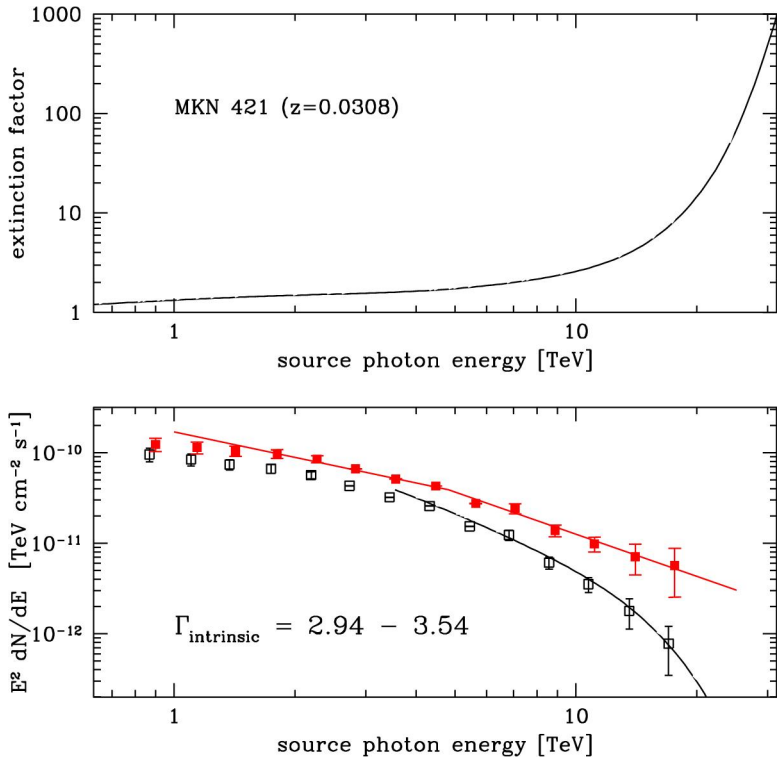

Figure 1.11: Example of the spectrum in the very-high energy regime of the source MKN 421 at $z = 0.03$. *Top*: Evolution of the extinction factor with energy. *Bottom*: The observed (black) and absorption-corrected (red) spectrum [14].

1.3 The blazar PG 1553+113

PG 1553+113 is the source that is characterized in this thesis. It is a high-frequency peaked BL Lac (HBL) object with a high luminosity and prominent activity. It is located at coordinates RA, Dec = (238.93 deg, 11.2 deg) (in the International Celestial Reference System, ICRS), with a redshift equal to z=0.433 [15].
This source has been long studied and monitored during the years across almost the entire electromagnetic spectrum, from radio to the very-high energy range (E> 100 GeV). Numerous **multi-band campaigns** have been conducted on PG 1553+113 and correlation studies have been performed.

A **correlation analysis** involves analyzing the variations in the flux across multiple energy bands simultaneously, to identify potential connections or dependencies between emissions in different parts of the electromagnetic spectrum. In this way, it is possible to validate emission models and make constrains on their parameters.

Typically, correlations are measured with correlation coefficients and the most widely used are the **Pearson correlation coefficient**, for **linear correlation** between two variables, and the **Spearman Rank Correlation Coefficient**, for **not linear** relationship. They commonly ranges from -1 and 1. A positive value of the coefficient indicates a *positive correlation*, meaning that as one variable increases, the other one tends to increase as well. A negative value indicates a *negative correlation*, meaning that as one variable increases, the other one tends to decrease. A *null correlation* means that there is no relationship between the variables.

In this kind of analysis, the correlation coefficient is associated with the **p-value**, which indicates the probability of obtaining a correlation. A low p-value suggests that the correlation is statistically significant, meaning that it is unlikely to have occurred by chance.

A comprehensive correlation analysis, involving all the available data bands analysed over the years, was performed for PG 1553+133 by the MAGIC collaboration [16] and the *preliminary* results are shown in Table 1.12. The source exhibits a **strong correlation** between the following energy bands:

- optical/UV
- optical/IR
- optical/High-Energy (HE)
- X-ray/Very-High Energy (VHE)

A **midler correlation** between:

Band-1	Band-2	Spearman Coeff.	p-value	panel
Optical	UV	0.94	4e-88	a
Optical	IR	0.90	2e-50	b
UV	HE γ-ray	0.66	3e-10	
Optical	HE γ-ray	0.63	2e-14	c
UV	VHE γ-ray	0.62	9e-08	
IR	HE γ-ray	0.61	1e-05	
X-ray	VHE γ-ray	0.60	6e-08	d
IR	UV	0.60	4e-06	
UV	X-ray	0.55	6e-18	e
Optical	X-ray	0.37	4e-08	f
HE γ-ray	VHE γ-ray	0.39	0.006	g
Optical	VHE γ-ray	0.35	2e-05	h
X-ray	HE γ-ray	0.32	0.006	i
IR	VHE γ-ray	0.26	0.09	
IR	X-ray	0.29	0.02	

Figure 1.12: The values of the *PRELIMINARY* results from the correlation study [16]. The Spearman Coefficient and the p-value for PG 1553+113 are listed in Table. *Thanks to the MAGIC collaboration.*

- X-ray/UV

and only a **hint of correlation** between:

- HE/VHE
- optical/X
- optical/VHE

These results suggest a **common origin** for the emission in IR, optical, UV and high-energy bands. IR, optical, and UV photons are likely synchrotron photons originating from the same emitting region. The **single-zone SSC process** is a feasible mechanism connecting optical and high-energy γ-ray photons. The same process may also be responsible for the X-ray to very-high energy γ-ray connection even though the radiation might come, at least partially, from a different (or additional) region compared to the low-energy counterpart, explaining the weaker correlation with other bands [16].

Moreover, PG 1553+113 is among the few blazars whose flux variability is claimed to be **periodic**. This topic will be discussed in Chapter 5, where light curves extracted from data collected in the high-energy and X-ray bands will be presented.

The features in the high-energy γ-ray light curve of PG 1553+113 strongly point to dynamics of a **binary system** of two supermassive black holes (SMBHs), with mass around $10^7 - 10^8 \mathrm{M}_\odot$ [17].

Chapter 2

Very High Energy Astrophysics

The γ-ray astrophysics is tipically divided in several energy ranges:

- High Energy (HE) (0.5 MeV - 100 GeV),
- Very High Energy (VHE) (100 GeV - 100 TeV),
- Ultra High Energy (UHE) (100 TeV - 100 PeV),
- Extreme High Energy (EHE) (above 100 PeV).

This thesis focuses on the energetic phenomena occuring in the VHE domain. Within this energy range, **non-thermal** phenomena are investigated, including Supernova (SNs) explosions, Supernova Remnants (SNRs), Pulsars (PSRs) and accretion in Black Holes (BHs). Among these, extragalactic sources of VHE γ-rays are AGNs and extreme transient events such as Gamma-Ray Bursts (GRBs) and SNs explosions. By observing the VHE radiation it is possible to investigate acceleration mechanisms and processes that produce the emission, study particles interaction with their surroundings, understand the role of magnetic field and all those physical phenomena that have remained poorly understood so far since they belong to the part of the electromagnetic spectrum that presents one of the most challenging investigation. In the exploration of the VHE processes domain, the **advantage** of studying γ-rays compared to charged particles as cosmic rays, is that they are not deflected by magnetic fields during their propagation, allowing to a proper characterization of the source, particularly regarding the direction of emission and the source localization. However, to observe in this energy band significant **challenges** must be overcome:

- the number of known VHE sources compared to other energy bands is relatively small, then statistics is limited;
- the emitted flux globally decreases with increasing energy; in the case of extragalactic sources this decrease is due to the γ-ray attenuation discussed in Section 1.10;

- VHE γ-rays are relatively rare compared to lower-energy photons, resulting in fewer detectable events;
- the background noise, including cosmic rays and atmospheric particle showers, could affect significantly the observations.

As a result, high-performance detectors and refined imaging systems are required to capture and measure this radiation, leading to an important technical challenge.

The limitation on the flux requires **longer exposure times** and sensitive detectors to accumulate sufficient data for analysis, in addition to sophisticated data filtering methods to distinguish the faint γ-ray signals from the background.

Generally, ground-based VHE detectors are located at high altitudes to minimize atmospheric absorption and reduce the luminous background originating from populated areas.

The atmosphere is not transparent to VHE γ-radiation. For this reason, the atmosphere is considered as an integral part of the instrument, specifically as a **natural calorimeter**. When a VHE γ-ray from space enters in the Earth's atmosphere, it generates a "cascade" of secondary particles, that detectors use to **indirectly detect** primary γ-ray properties.

The specific dynamics of atmospheric showers are treated in Section 2.1. Then, in Section 2.2 is discussed the Cherenkov radiation and in Section 2.3 the specific technique used to detect atmospheric showers.

2.1 Extensive Air Showers

When a relativistc charged particle or VHE γ-ray enters in the atmosphere produces Extensive Air Showers **(EAS)**, a cascade of particles generated by their interaction with atmospheric nuclei. This phenomenon is utilized to indirectly detect γ-rays and cosmic rays. EAS can be of two types, depending on the nature of the *primary particle*:

- *electromagnetic (EM) showers*, initiated by high-energy γ-rays or electrons,
- *hadronic showers*, initiated by cosmic rays, mostly consisting of protons ($\sim 90\%$) and heavier nuclei.

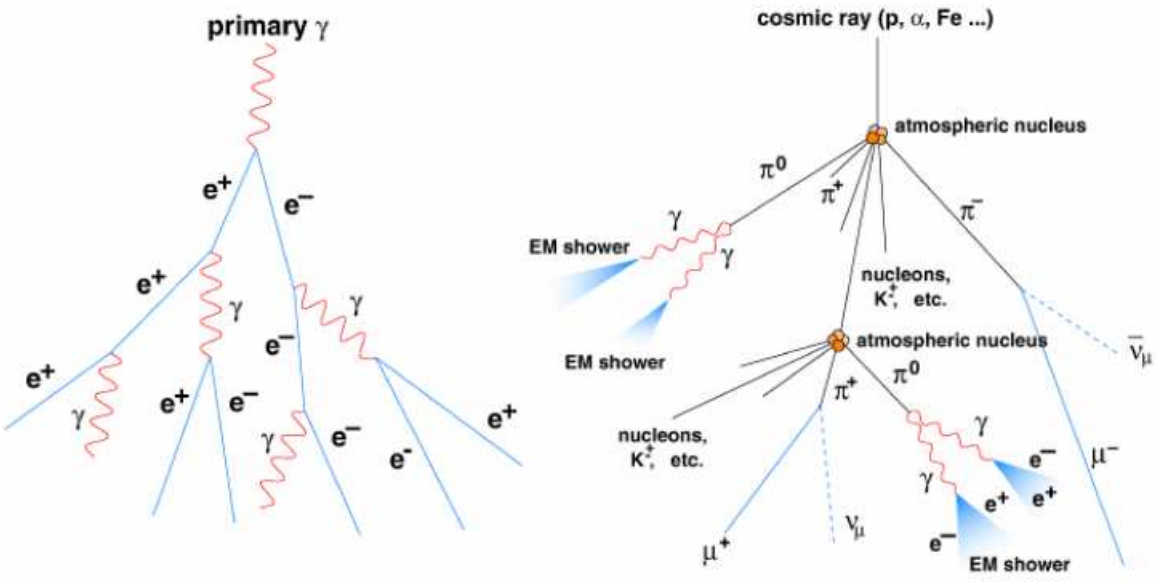

Figure 2.1: Schematic representation of electromagnetic (*left*) and hadronic cascades (*right*) [5].

An **electromagnetic shower** is produced by a particle that interacts primarily or exclusively via the electromagnetic force, usually a photon or electron. Considering the photon case: when it enters in the Earth's atmosphere with an energy that generally is in the GeV-TeV range, it interacts with the electric field of atomic nuclei at a typical altitude ranging from 5 to 30 km, and it undergoes **pair production**:

$$\gamma_{VHE} \rightarrow e^- + e^+ \tag{2.1}$$

Successively, electrons and positrons emit **Bremmstrahlung** photons. Then, those photons convert again into pairs and so on. The longitudinal development of the EM shower is very well described by the *Heitler model* [18], an analytical approximation which neglects additional processes like multiple scattering of charged particles and $e^{\pm}$ energy losses by ionization and assume a single photon production in the Bremmstrahlung process. The model predicts that at each step the energy is shared with produced particles, which will have on average an energy equal to $E(t) = E_0/2^t$, where E_0 is the primary energy of the photon and t is the number of steps. The multiplication process continues as long as the *critical energy* is reached, namely the energy below which the emission by collisions dominates on the Bremmstrahlung process, that in the air is about ~ 84 MeV. Tipically, the duration of an EM shower is of the order of few nanoseconds.

The development of a **hadronic shower** occurs when a high-energy hadron, such as a cosmic ray (CR) with a primary energy tipically between $10^{14} - 10^{17}$ eV, interacts with the

nucleus of an atom in the atmosphere via strong nuclear force. This interaction induces a complex chain of **secondary particles** production. The first products of a shower induced by an hadron are **charged pions**, that decay producing **muons** and **neutrinos**:

$$\pi^+ \rightarrow \nu_\mu + \mu^+ \tag{2.2}$$

$$\mu^+ \rightarrow \overline{\nu}_\mu + \nu_e + e^+ \tag{2.3}$$

(same processes occur for π^- and μ^- with opposite-charged products) and **neutral pions** that decay in two HE gamma-rays:

$$\pi^0 \rightarrow \gamma_{HE}\gamma_{HE} \tag{2.4}$$

that generate electromagnetic sub showers similar as described before.

The shower stops when the *critical energy* is reached, namely the energy at which pions are more likely to interact rather than decay, and in air it is around ~ 20 GeV. This shower development is more complex than EM shower since the number of secondary particles is much bigger, leading to a **more extensive** shower with a **longer duration**, typically of tens nanoseconds.

The large distribution of hadrons arriving isotropically in the atmosphere, in a quantity that is *three order of magnitude higher* than γ events, represents a **significant background** source that should be subtracted in various experimental settings. The differences between EM and hadronic showers are used to discriminate γ-ray/hadron initiated showers.

For both these showers it is possible to investigate geometrical properties and get the most relevant information:

- the **nature** of the primary particle,
- the **primary energy**,
- the arrival **direction**.

2.2 Cherenkov radiation

Cherenkov radiation is a phenomenon that occurs when a charged particle travels through a medium at a speed exceeding the velocity of light in that medium.

It results in the emission of **optical/UV** electromagnetic radiation peaked in the *blue* part of the spectrum, producing light-cone flashes. Key properties of Cherenkov radiation are:

- radiation is emitted in a **cone-like pattern** with the peak in altitude tipically around ~ 10 km corresponding to the maximum shower development;

- the **opening angle** θ_c of the cone is determined by the particle's velocity in the medium:

$$\cos\theta_c = (\frac{1}{\beta n}) \leq 1 \tag{2.5}$$

  where n is the refraction index and β is equal to v/c. From this equation, the constrain on the velocity is derived:

$$v \geq \frac{c}{n}; \tag{2.6}$$

- the radiation is emitted during all the shower development, in the **forward direction**;
- the duration of the compact light pulse lasts for less than a **nanosecond**.

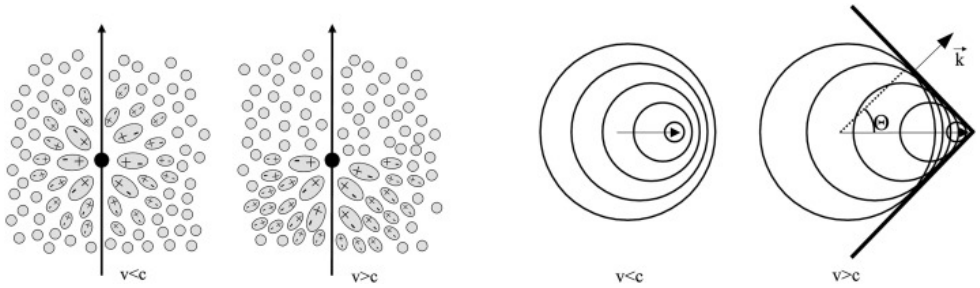

Figure 2.2: (*Left*) Illustration of a medium polarized by a relativistic particle. (*Right*) Schematic representation of the Cherenkov wave-front formation [19].

In an EM shower, the Cherenkov radiation is produced by electrons and positrons generated by the primary photon. This process represents the most suitable way to detect properly VHE γ-ray events.

2.3 Imaging Atmospheric Cherenkov Telescopes (IACTs)

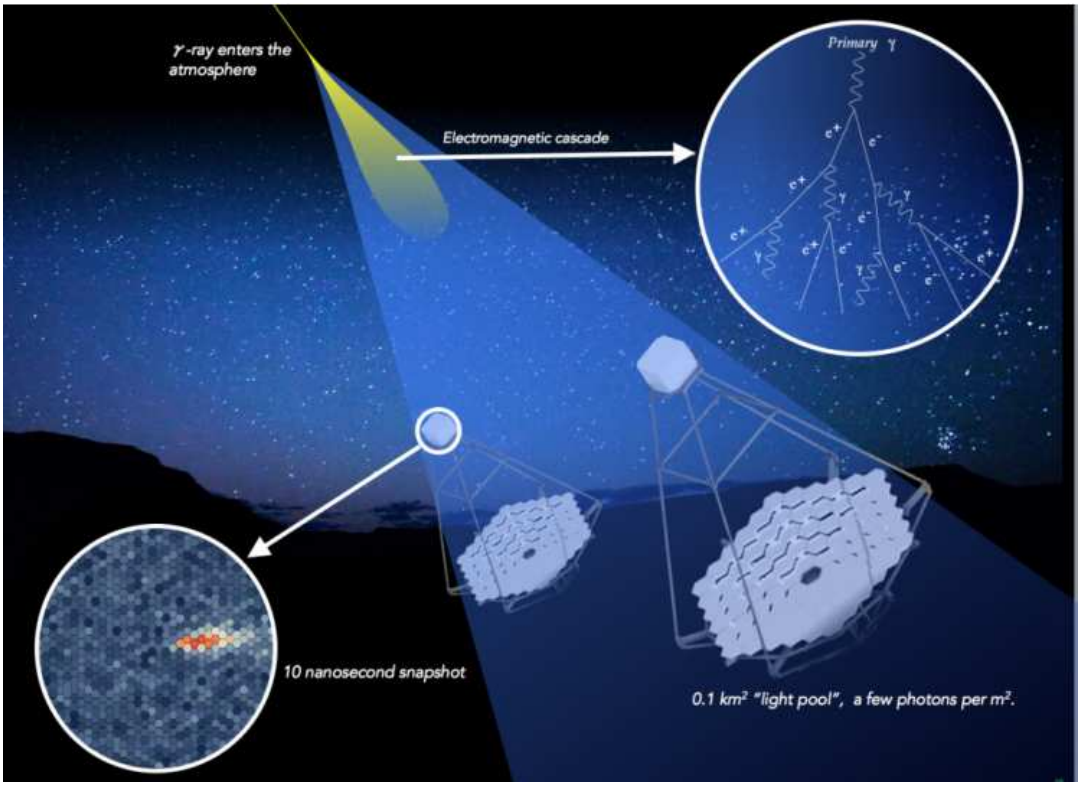

Figure 2.3: Scheme of the imaging atmospheric Cherenkov technique. From: https://www.cta-observatory.org/about/how-cta-works/.

Specialized instruments designed to collect VHE γ-rays through the detection of Cherenkov radiation emitted by EAS are the **Imaging Atmospheric Cherenkov Telescopes (IACTs)**. A IACT consist of a **large segmented mirror**, typically with a diameter of 10-20 meters, designed to collect Cherenkov light and reflect it onto a **camera** located at the focal plane. The camera of an IACT is composed of an array of sensitive **Photomultiplier tubes (PMTs)** or other fast light detectors like Silicon Photomultipliers **(SiPM)**. The number of PMTs of the current IACTs is more than a thousand, depending on the size and design of the telescope. A **fast timely response** is needed to register fast Cherenkov flashes.

The camera is equipped with a sophisticated **trigger system**, programmed to activate when 3 or 4 adjacent pixels simultaneously register a signal, known as a coincidence. This logic system examines **temporal coincidences** of adjacent pixels, rapidly making the critical decision of accepting or rejecting an event: by setting a discrimination threshold for each pixel, the signals in the trigger branch become digital. The trigger identifies the **presence of a shower** compared to the background noise from the diffuse light of the sky, without distinguishing between electromagnetic and hadronic showers. This distinction is made in

the subsequent image analysis.

The recorded data includes information about the intensity and arrival times of the detected photons, as well as the pixel positions on the camera. These information allow for the reconstruction of the shower and primary γ-ray properties. This approach has completely changed the field of VHE γ-ray astronomy, introducing a technique that allows for the detection and study of VHE γ-rays. Before the development of IACTs, there was no efficient and reliable way to detect signals in the VHE regime.

Currently, IACTs in operation are:

- **H.E.S.S.** (High Energy Stereoscopic System), that observes from $\sim$200 GeV to several tens of TeV. Installed in Namibia, comprises a square arrangement of four 12-meter telescopes, creating a 120-meter side length, supplemented by a central fifth mirror measuring 28 meters.

- **VERITAS** (Very Energetic Radiation Imaging Telescope Array System), an array of four 12 meters optical reflector located in Arizona, that covers the energy range from about 85 GeV to more than 30 TeV.

- **MAGIC** (Major Atmospheric Gamma-ray Imaging Cherenkov Telescopes), composed by two telescopes of 17-meters diameter located in La Palma (Canary Islands), operating in approximately 50 GeV - 50 TeV range.

- **LST-1** (Large-Sized Telescope), part of the Cherenkov Telescope Array, situated in La Palma (close to MAGIC), with a 23 meters mirror, more sensitive to energies from about 20 GeV to $\sim$150 GeV.

While the upcoming projects are:

- **CTA** (Cherenkov Telescope Array) designed to cover an extended energy range, with the low-energy array spanning from around 20 GeV to 300 GeV and the high-energy array reaching from a few tens of GeV up to over 100 TeV.

LST-1 and CTA will be described in detail in Chapter **??**.

2.4 IACT's properties and observation modes

To be efficient, IACTs require some observational conditions to be fulfilled. Since they are essentially optical telescopes, **dark conditions** are needed during data collection to minimize the contribution from the **Night Sky Background (NSB)**. Moreover, due to the relatively

small Field of View (FoV) of the instruments (usually less than $\sim 5^{\circ}$) [20], they should point directly the source to observe to collect as many photons as possible.

These circumstances are recommended for a better **sensitivity**, which is tipically defined as the lowest detectable flux to have a 5σ significance, in a specific energy bin, in 50 hours of observation.

Another significant quantity to be defined is the **angular resolution**, which refers to the ability of the telescope to precisely determine the arrival direction of a γ-ray. A smaller angular resolution corresponds to a more precise localization of the source position in the sky.

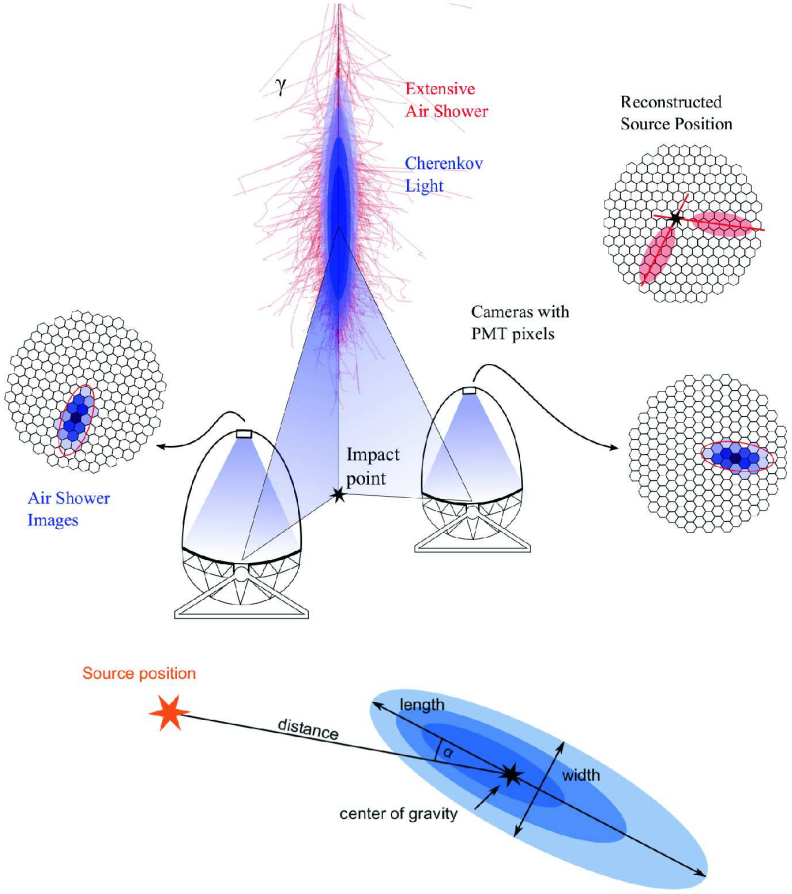

Figure 2.4: Reconstruction of the source position from a signal belonging to the same shower detected by two telescopes [21].

A powerful tool to significantly improve the sensitivity, the angular resolution and the background rejection in the analysis is to perform **stereoscopic observations**, using multiple telescopes in an array to observe the same shower development. This allows to reconstruct better the geometrical properties of the shower, in particular providing more accurate calculations on the arrival direction, as shown in Fig. 2.4.

The performance of the IACTs is influenced by observational conditions but also by **hard-**

ware capabilities. An important factor to consider is the **energy threshold**, that refers to the minimum energy of γ-rays that the telescope can detect with reasonable efficiency. This threshold is affected by hardware properties like PMTs efficiency and reflector size, as well as the **zenith angle** of the observations. Showers arriving from higher zenith angles travel a longer path through the atmosphere, resulting in a *larger light poo*l but *lower Cherenkov photon density* and increased *atmospheric attenuation.* As a consequence, low-energy γ-rays may not be detected by the telescopes, leading to an increase in the energy threshold. However, a larger collection area enables the detection of γ-rays up to several tens of TeV. The **effective collection area** A_{eff} is defined as the area within the instrument can effectively detect a γ-ray. A_{eff} is determined by Monte Carlo (MC) simulations, considering the size of the Cherenkov light pool, the energy of the γ-ray and the zenith angle at which it enters in the atmosphere. It depends also on the specific design and characteristics of the IACT. Generally, it is of the order of magnitude of $\sim 10^5$ m^2. In formula, the effective area is defined as:

$$A_{eff} = \int P(x, y, E) dx dy \tag{2.7}$$

where P(x,y,E) is the probability to observe a γ-ray with energy E at a distance x,y from the telescope axis.

Chapter 3

The Cherenkov Telescope Array

The Cherenkov Telescope Array (CTA) will be the most advanced IACT in operation.

The array will be developed in two sites, one located in La Palma in the Canary Islands, and one at the European Southern Observatory (ESO) site in Paranal, Chile. The distribution of telescopes in both the northern and southern hemispheres enables a complete sky coverage. The array will consist of three classes of mirrors having different size, to cover a wide energy range, from $\sim$20 GeV to $\sim$300 TeV.

At the **lowest energies** (E$\leq$ 150 GeV), γ-ray events are abundant but the Cherenkov flashes produced by initiated showers are faint. Therefore, large light-collection areas are required to collect as much light as possible. At the **highest energies** (E> TeV), γ-ray photons are rare due to the decreasing nature of emission mechanisms with energy. In the case of extragalactic sources, the EBL absorption significantly accentuates this phenomenon. Therefore, many telescopes are needed to cover a large detection area and increase the possibility to observe γ-ray events. Showers induced by a γ-ray at these energies are more extensive, resulting in brighter and well-defined signals from Cherenkov flashes. For this reason, a smaller mirror area with respect to the previous one can be adopted.

The main difference between the two energy ranges is that the lowest one is limited by the large background, instead the highest one is restricted by the statistics.

These considerations lead to a design where array will be formed by a few **Large-Sized Telescopes (LSTs)**, tens of **Mid-Sized Telescopes (MSTs)**, and a large number of **Small-Sized Telescopes (SSTs)**.

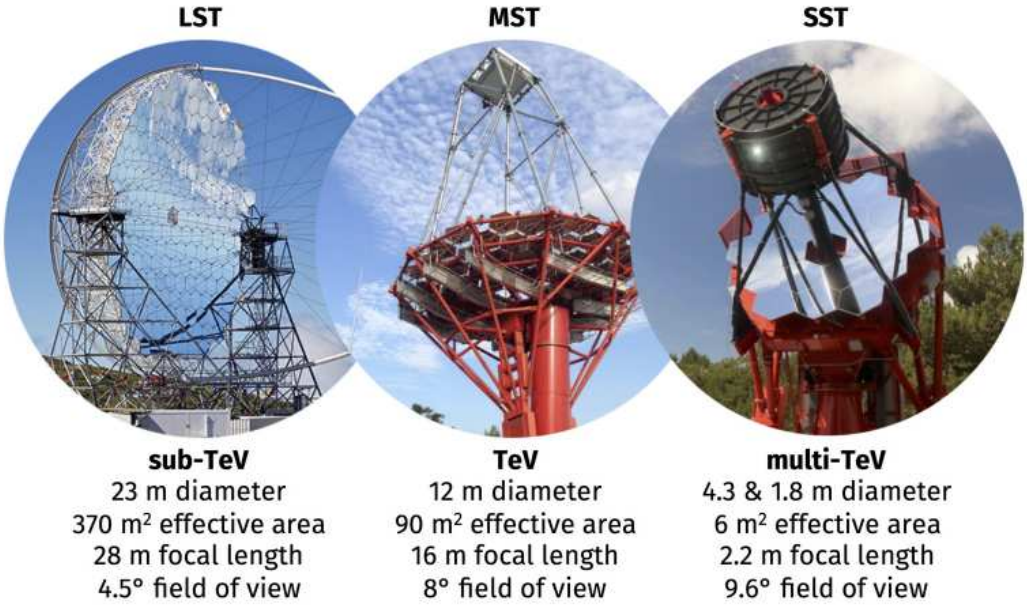

Figure 3.1: The three telescope types of CTA. The Large-Sized Telescope (LST; left) is optimised for sub-TeV energies, the Mid-Sized Telescope (MST; centre) is optimised for the TeV range, and the Small-Sized Telescope (SST; right) is optimised for multi-TeV gamma-ray photons [22].

The specific number of the different telescope types is: 14 MSTs and 37 SSTs in the South, and 4 LSTs and 9 MSTs in the North, as described in the *Alpha Configuration* [23]. The Northern array is optimized for the low to medium energy range (20 GeV – 5 TeV), and it will specialize in extragalactic source and transients. The Southern array will focus on Galactic targets, providing the oppprtunity to investigate the Galactic Center, that is well visible from this hemisphere. The array is optimized for the medium and high energy range (150 GeV – 300 TeV), making it particularly well-suited for studying PeVatron sources and delving into particle acceleration mechanisms.

The capability of CTA for the detection of γ-rays will depend strongly on the effective collection area, estimated by MC simulations developed for the North and South sites and shown in Fig. 3.2, taking into account cuts optimised to maximize the sensitivity.

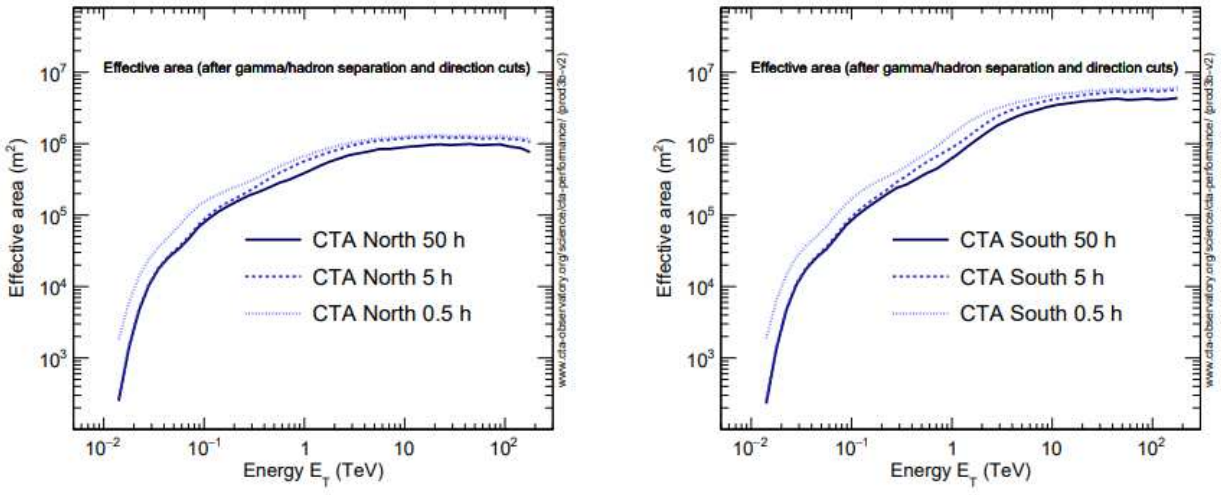

Figure 3.2: Effective collection area for point-like gamma-ray sources for CTA North (left) and CTA South (right). Especially notable is the sensitive area of several thousands of m^2 in the threshold region around 30 GeV [24].

The purposes of the array are [25]:

- improve the sensitivity level by an order of magnitude at 1 TeV (see Fig. 3.3),
- significantly increase the detection area and hence photon rate, providing access to the shortest timescale phenomena,
- substantially improve angular resolution and increase the field of view to image extended sources (see Fig. 3.4),
- provide a very wide range of energy, from ∼20 GeV to ∼300 TeV,
- enable the entire sky coverage.

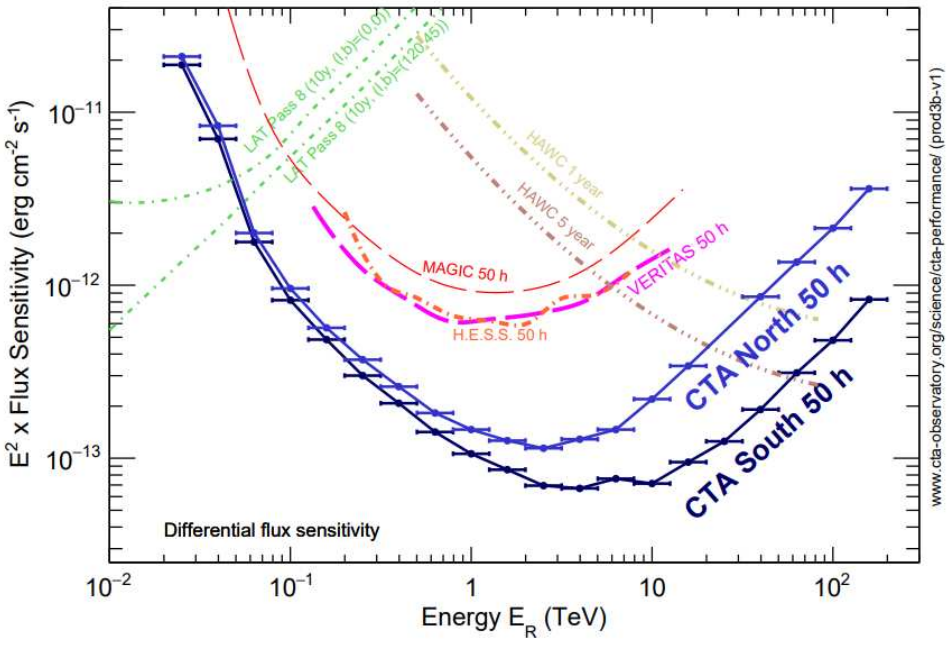

Figure 3.3: Differential energy flux sensitivities performed by MC simulations for CTA (South and North) compared with the performance of existing γ-ray instruments [25].

Some of the main **scientific questions and topics** that will be investigate by CTA are [25]:

- understanding the origin and role of relativistic cosmic particles,
- probing extreme environments, like black holes and jets, neutron stars and relativistic outflows,
- search for Dark Matter (DM) signatures and Axion-Like Particles (ALPs),
- studying deeply the Galactic Centre (GC) and the diffuse VHE emission,
- providing a map of VHE galactic sources (already done in other wavelengths),
- extragalactic survey to investigate extreme Blazars, Radio-Galaxies, Gamma-Ray Bursts, Starbust Galaxies, Dark Matter Clumps and new class of possibly existing sources,
- improve the cosmological constraints obtained with blazars on the diffuse EBL.

An important aspect of CTA will be its capability to react to **alerts**. The TeV sky can be extremely variable and the CTA Observatory will possess the ability to receive alerts from external observatories, as well as generate alerts during its observational activities. This will

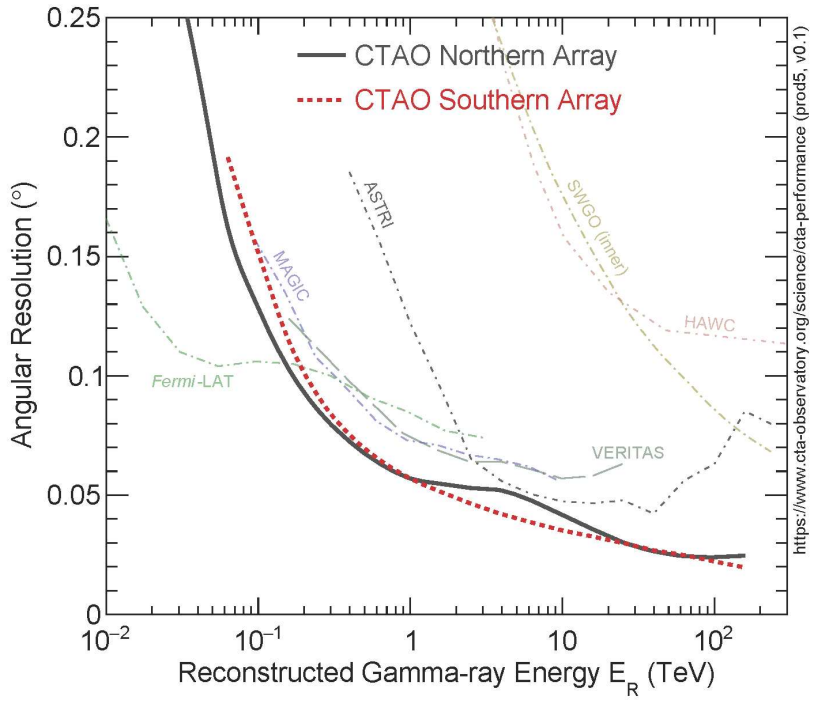

Figure 3.4: CTA angular resolution compared to other instruments, latest performance plot from *https://www.cta-observatory.org/science/cta-performance*.

give CTA the opportunity to have important synergies with many of the current and new generation of astronomical and astroparticle observatories (such as Fermi for the HE band, IceCube and KM3NeT for neutrino observations, LIGO and Virgo for gravitational waves), contribuing to **multi-wavelength (MWL)** and **multi-messenger (MM)** studies.

3.1 The Large-Sized Telescope (LST)

The Large-Sized Telescope prototype (LST-1), was inaugurated in 2018 and collected its first light in December 2018 [26].

Figure 3.5: LST-1 in La Palma, Canary Islands.

LST-1 is shown in Figure 3.5. The 23-meter parabolic mirror corresponds to a surface of 400 m^2, designed to improve sensitivity at the lowest energies, making it suitable for observations between $\sim$20 to $\sim$150 GeV. To compensate for small dish deformations at different zenith angles, the mirror is provided with an Active Mirror Control system. The reflective surface collects and focuses the Cherenkov light into the **camera**, equipped with 1855 photo-sensors. Each photo-sensor converts light in electric signal, which is processed by the dedicated readout electronics. The instrument has a field of view of 4.5° and a **fast repositioning** within 20 seconds, that allows to react to transient phenomena and capture brief and fast Cherenkov flashes [27].

The LSTs cameras will be interconnected in order to form an hardware coincidence trigger among the telescopes, which is useful to suppress accidental triggers by up to a factor of 100 [20]. The trigger helps to distinguish between a γ-ray like signal and background noise. A shower can be recognized from its topology and temporal evolution. A γ-ray induced signal can be identified because EM showers generate elliptical and narrow images, while hadron showers produce irregular and wide signals on cameras. Moreover, secondary particles like muons produce clear ring-like images that are easy to identify during the data analysis (see Fig.3.6).

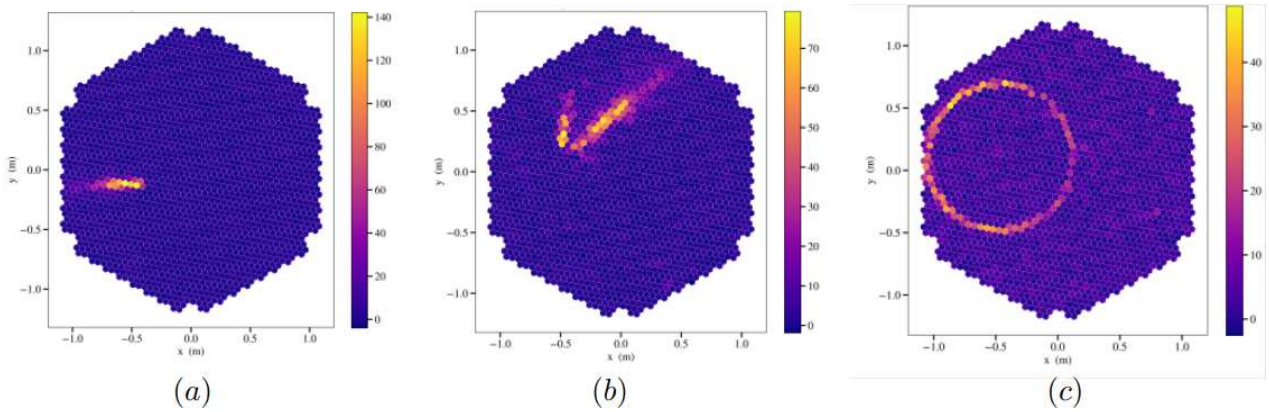

Figure 3.6: Different types of images recorded by LST-1. (a) A γ-ray candidate; (b) a shower with two EM sub-showers, most likely initiated by a cosmic-ray proton; (c) a muon ring [28].

Three more LSTs are planned to be built in the same site in next few years (see Fig.3.7). Currently, LST-1 does **joint observations** with MAGIC, located in the same site, for a comprehensive and complementary approach, to have a broader coverage of the VHE γ-ray energy spectrum and to confirm the accuracy of the data with cross-verification, reducing the chances of systematic errors.

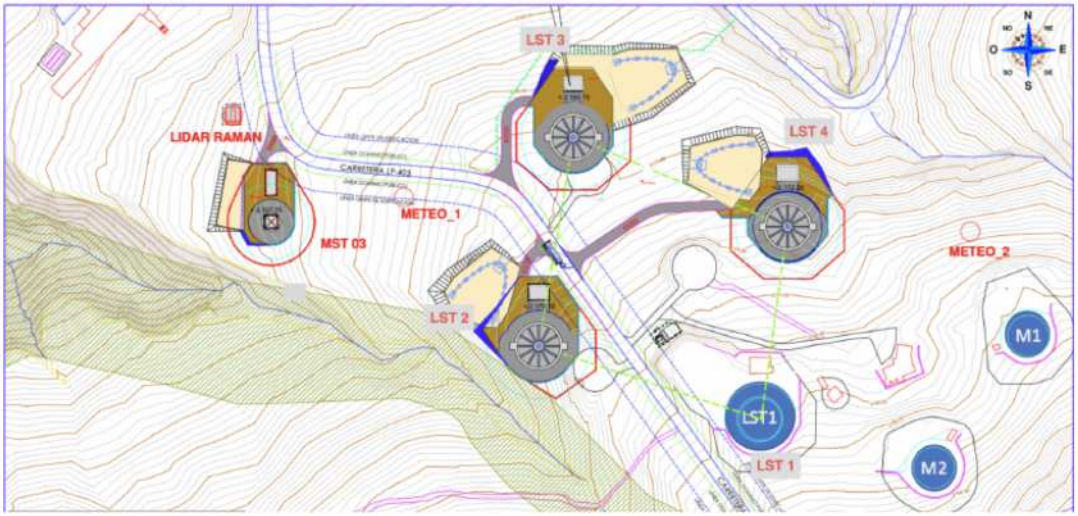

Figure 3.7: Future location of LSTs in the CTA North site [27].

3.2 LST-1 analysis pipeline

The objective of this section is to introduce the LST's data analysis technique, describing the entire analysis pipeline from the initial low-level steps (trace integration, image cleaning, shower parameterization, etc.) to the higher-level analysis (source detection, flux estimation,

etc.). The analysis is performed with **cta-lstchain**, the pipeline software based on **ctapipe**, the framework for prototyping the low-level data processing algorithms for the CTA. The high-level analysis is performed with the high-level gamma-ray tool **Gammapy**.

In the next section are described all the data levels, from the acquisition to the calibration. Then, a comprehensive discussion on the background estimation is done in Section 3.2.3. The two type of analysis that can be performed, source-dependent and source-independent, are discussed in Section 3.2.2.

3.2.1 LST-1 data levels

LST-1 data levels follow the common data reduction workflow that can be inferred for VHE γ-ray telescopes. In particular, LST data can be divided into:

- **R0**: unprocessed data directly acquired from the detectors.
- **R1**: preprocessed version of the recorded data, processed and calibrated to remove instrumental effects and convert the signals into meaningful units.
- **DL0**: starting point for subsequent data processing, consisting of digital samples from the readout electronics that contains the Cherenkov signal.
- **DL1a**: preprocessed and partially calibrated dataset, corrected for instrument effects, such as pixel gain variations and time offsets.
- **DL1b**: calibrated and reduced dataset, includes information such as calibrated arrival times, charge measurements, image parameters and other relevant observables.
- **DL2**: dataset contains various parameters and information, such as arrival direction, reconstructed energy, background and gammaness (a probability of an event being a γ-ray candidate), estimated using Machine-Learning (ML) methods.
- **DL3**: event list of selected γ-ray-like events.
- **post-DL3**: scientific results are produced, such as Fluxes, Spectra, Light Curves, making use of high-level analysis tools.

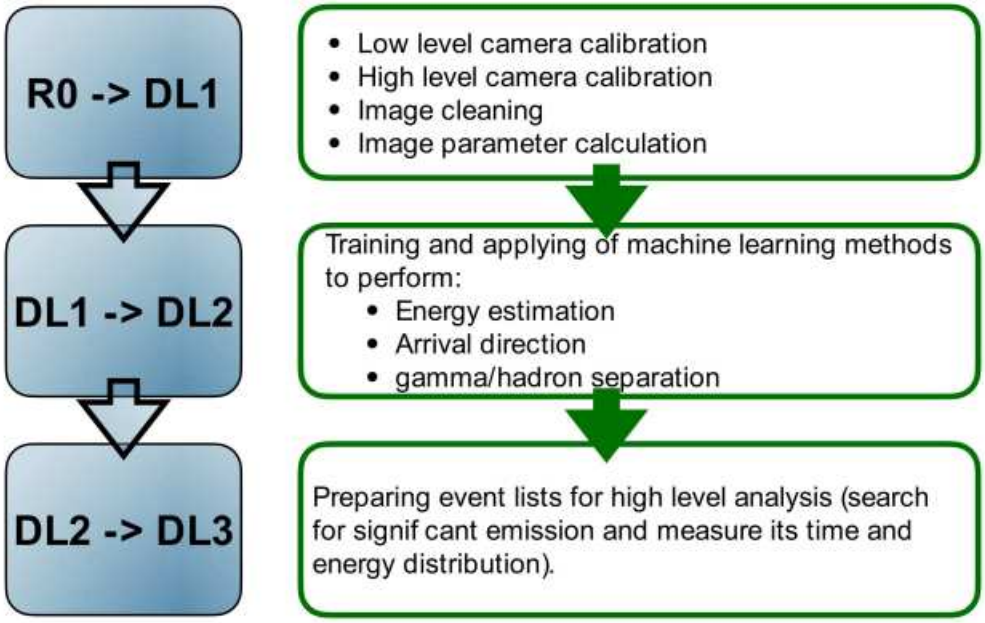

Figure 3.8: The analysis workflow for LST-1 data generated by *lstchain*. The initial raw inputs undergo processing steps until a list of γ-ray candidates is obtained. Subsequently, additional data processing can be carried out using the available high-level gamma-ray analysis tools [29].

3.2.2 Source-dependent and source-independent analysis

Two kinds of analysis can be performed: a source-dependent or a source-independent analysis. The difference between source-dependent and source-independent analysis lies in how data are processed and analyzed in the context of data reconstruction and calibration.

In a **source-dependent** analysis, data are specifically adapted to study and extract information from a particular γ-ray source or a group of sources. The analysis focuses on a predefined region of interest containing the target sources, and the parameters and models used for data analysis are customized to fit their characteristics. Source-dependent analysis aims to maximize sensitivity and optimize the detection of γ-rays from the selected region, but this kind of approach requires **prior knowledge** of the sources and may not be applicable outside the predefined region of interest. Anyway this method has its advantages, since it works well for the case of **single-telescope observations**, in which it is slightly more complex and less precise to reconstruct the shower geometry compared to observations with multiple telescopes [30]. This approach has a better performance in energy reconstruction and γ/hadron separation at energies below $\sim$100 GeV, leading to a higher sensitivity compared to the source-independent approach (see Fig.3.9) [31].

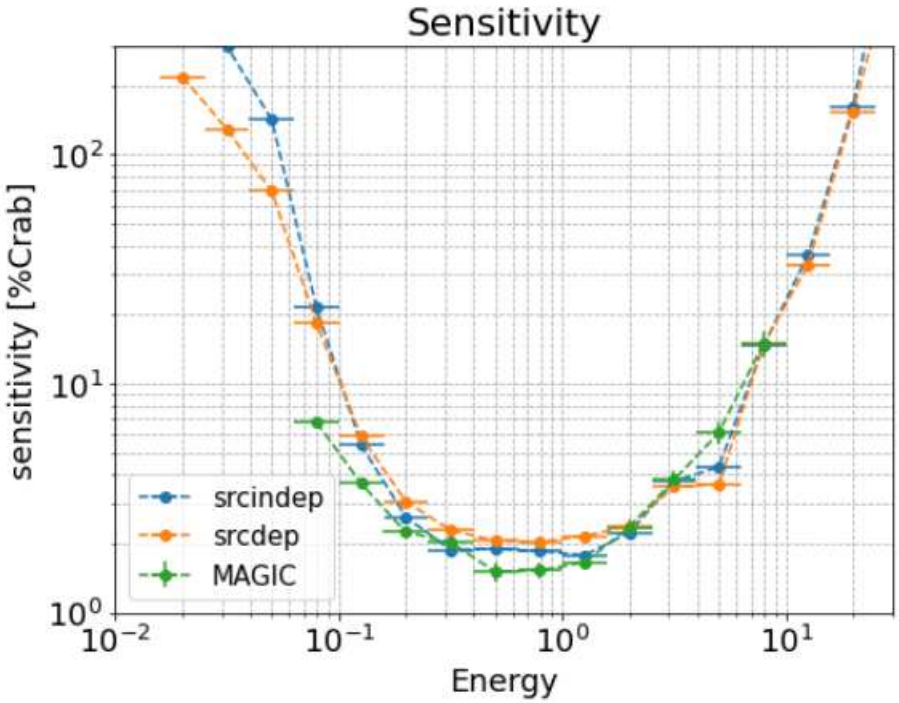

Figure 3.9: Comparison between sensitivity in function of energy (TeV) in source-dependent (orange), source-independent (blue) LST analysis and MAGIC analysis (green) [31].

In a **source-independent** analysis, data are processed and analyzed without any prior knowledge about a specific γ-ray source. This is the standard method applied in IACT observations. The analysis is performed using a more general approach and it aims to provide a more comprehensive understanding of the emitting region characteristics, accounting for background properties and instrumental response. In terms of performance, this approach works better at middle/high energies, with an enhanced background rejection [31]. In this thesis, a source-independent analysis is performed.

3.2.3 Background estimation

The background estimation is a crucial step in the VHE data analysis. The following description is taken by [32], which describes in detail the background modeling in VHE γ-ray astronomy.

Observations are taken using the **wobble mode**, which consists in continuously keeping the target source region within the FoV, while applying an alternating offset relative to the pointing direction. By using a region positioned on the opposite side of the FoV within the same run, it is possibile to obtain a background estimation (**OFF data**) for the source region (**ON data**). Given a number of counts N_{on} in an ON-region and N_{off} counts in a background

region, the γ-ray excess is defined as:

$$N_{excess} = N_{on} - \alpha N_{off} \tag{3.1}$$

where α is a normalisation factor that takes into account discrepancies between the ON-region and the background region. N_{excess} represents the number of γ-*ray-like* events.

One commonly used background estimation method is the **ring background** technique. It involves selecting a ring-shaped region centered around the source position and measuring the average count rate within this region (see Fig.3.10). The assumption is that the counts within the ring predominantly arise from the background, while the excess counts associated with the source are concentrated at the source position. By subtracting the estimated background counts from the total counts, the signal from the source is measured.

Another technique is the **reflected-region background**, which consists in reflecting the ON region relative to the center of the FoV (here is the observation position, not the source position as before) to generate a single OFF region. In the typical scenario, multiple reflected OFF regions are positioned within the ring, avoiding the vicinity of the trial source location to prevent background contamination from misidentified γ-rays (see Fig. 3.10). As both ON and OFF regions have equal offsets from the system's pointing direction, there is no need for a radial acceptance correction and α is simply $1/N_{off}$.

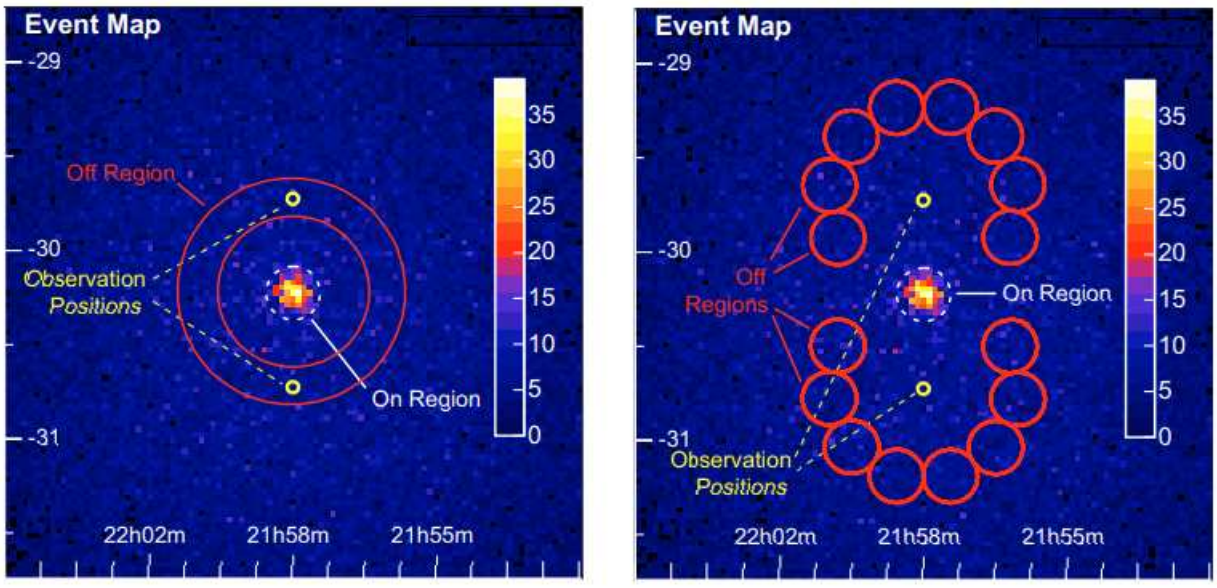

Figure 3.10: Illustration of the ring-background (*left*) and the reflected-region-background (*right*) technique [32].

Chapter 4

LST-1 analysis workflow

In this chapter are described in detail all the steps of the analysis, starting from the data selection in Section 4.1, calibration and parametrization in Sections 4.2, 4.4 and arriving to post-DL3 analysis in Section 4.5. A particular attention is dedicated to the instrument response function in Section 4.3 and to the theta-squared parameter, treated in Section 4.4.1.

4.1 Data selection

Data selection is applied to the calibrated dataset that includes information about relevant observables (**DL1b files**). Selection conditions are applied with the purpose of selecting observations that satisfy the required criteria. Initially, it is necessary to find runs during which the telescope was pointing towards the source of interest. For this purpose, referring to a catalog in which are collected all the observations with related information might be helpful. Subsequently, selections based on parameters has to be done. The desired range for the zenith angle and a reasonable angular distance from the pointing position can be chosen. In addition, it is necessary to exclude runs with too high noise and with too-low photon rate, that probably indicate non-optimal weather or telescope issues. It is useful to check Sun and moon position during the observation time, to spot datataken in twilight or moon conditions.
The result of this procedure is the final list of selected files to which apply the further analysis.

4.2 DL1 to DL2

DL1 files from previous selection are ready to be processed and transformed into DL2 format. Machine-learning algorithms, namely **Random Forests (RFs)**, have been developed to classify primary particles to be γ candidates or hadron background and reconstruct their energy and direction. RF models are trained with DL1 data that contain *Hillas parameters* [33]

(specified in the configuration file), which describe features of the Cherenkov image of the shower in the camera (see Fig. 4.1).

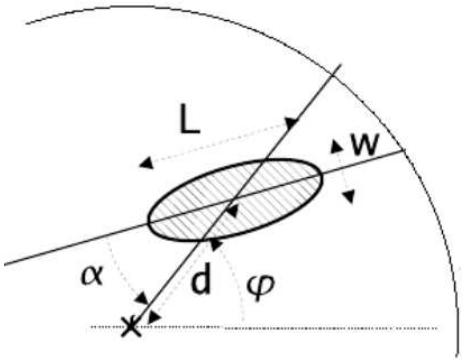

Figure 4.1: Geometrical definition of the Hillas Parameters. The γ-ray signal is identified as a two-dimensional ellipse. The Hillas parameters usually are: the length L and width w of the ellipse, the size (total image amplitude), the angular distance d between the centre of the camera and the image centre, the azimuthal angle of the image main axis ϕ, the orientation angle α [34].

These RF models are applied to DL1 data to transform them into **DL2**, using the script:

- `lstchain_dl1_to_dl2`

and they are used to perform:

- γ/**hadron separation**, the ability to correctly recognized and separated γ-ray events from hadronic events (background events).;
- **energy reconstruction**, the estimation of the energy of the primary γ-ray;
- **direction reconstruction**, the determination of the direction from which a γ-ray originated in space.

RFs can be trained for a wide range of telescope pointings (e.g. along the path of a given source in alt-az).

4.3 IRFs

The **Instrument Response Functions (IRFs)** describes the detector response to γ-rays at different energies and incident angles. They are obtained through a combination of MC simulations of γ-ray showers and calibration data [35]. Data from observations need to be

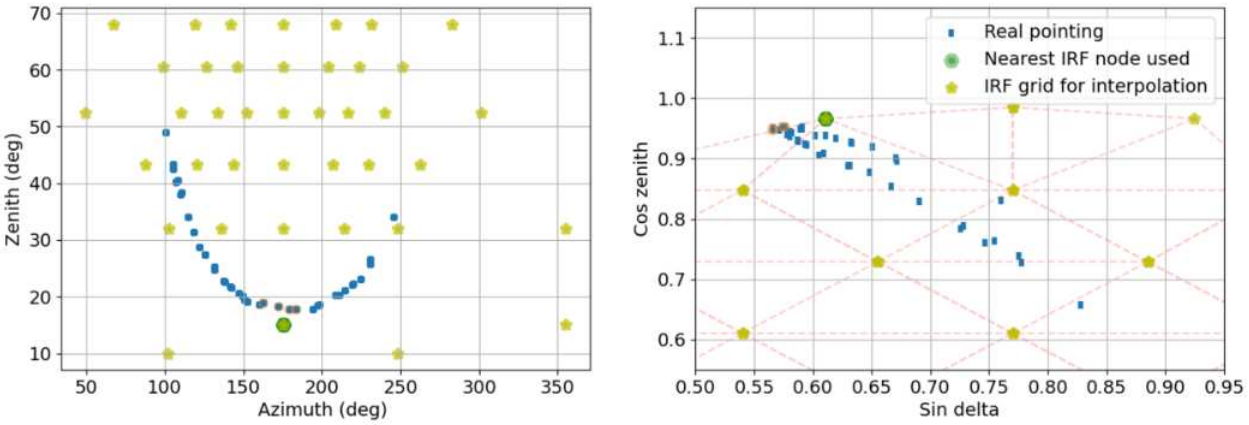

Figure 4.2: An almost uniform grid of sky position nodes for the Testing Dataset Monte Carlo is created for declination 9.31deg. *Left*: grid in azimuth and zenith angle. *Right*: grid in the space of cosine zenith and sine of the angle (delta) between the geomagnetic field and the particle shower direction. The IRFs interpolation was performed using *pyirf v0.7*. (Thanks to Dr. Chaitanya Priyadarshi)

combined with IRFs to translate reconstructed quantities (particle nature, arrival direction and primary energy) into a particle flux [35].

The IRF can be expressed mathematically through this formula:

$$\mathrm{IRF}(E, \Omega | E_{\mathrm{true}}, \Omega_{\mathrm{true}}) = A_{\mathrm{eff}}(E_{\mathrm{true}}, \Omega_{\mathrm{true}}) \cdot p_{\mathrm{PSF}}(\Omega | E_{\mathrm{true}}, \Omega_{\mathrm{true}}) \cdot p_{\mathrm{energy}}(E | E_{\mathrm{true}}, \Omega_{\mathrm{true}}) \quad (4.1)$$

where A_{eff} is the effective area (in m^2), p_{PSF} is the angular resolution (in sr^{-1}) and p_{energy} is the energy dispersion (in TeV^{-1}).

The **energy dispersion** is the difference between the detected and true energy.

MC simulations have been performed for a **grid of nodes** intended as a set of discrete positions in the sky defined in terms of azimuth and zenith angles (see Fig.4.2).

The purpose of creating a grid of nodes is to facilitate the interpolation of IRFs, allowing for more accurate results.

lstchain includes modules to estimate IRFs for each node, that can be done using the script:

```
- lstchain_create_irf_files
```

in which a flag '–point-like' (creation of IRFs for point-like sources) or '–diffuse' (creation of IRFs for extended sources, diffuse emission) can be specified, depending on the case of interest. In this analysis, '–point-like' IRFs are used.

They contain information about:

- **effective area**, proportional to the detection efficiency of γ-rays and computed as function of the true energy;

- **point spread function (PSF)**, the instrument angular response to a point-like source;
- **energy dispersion**, built from the dispersion energy matrix (ratio of the reconstructed energy over the true energy as a function of the true energy).

During the creation of IRFs, it is possible to specify some additional configurations, such as:

- perform a **source dependent analysis**,
- fix the efficiency to optimize γ/**hadron separation**,
- define the percentage containment region for **theta cuts**,

The γ/**hadron separation efficiency** is expressed in percentage. The higher is the efficiency, the harder is the cut, then the probability of losing γ-ray events increases.

Theta (θ) is the angular distance between the reconstructed direction of the incoming γ-ray photon and the position of the source, identified as the pointing direction of the telescope (see Fig. 4.3). Some cuts on θ to reject background contaminations can be applied during the analysis for a better γ-ray signal search.

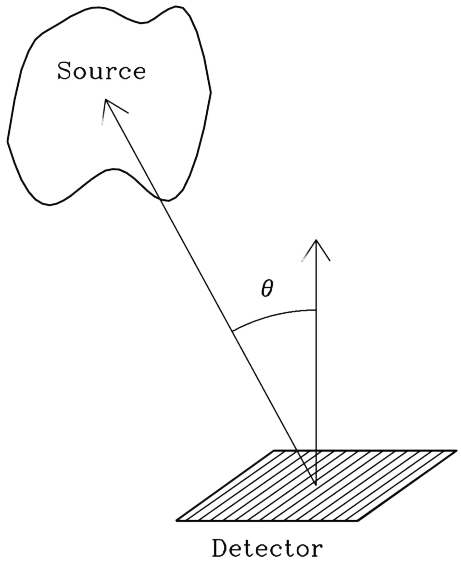

Figure 4.3: Schematic representation of θ. In figure are illustrated the telescope pointing direction and the position of the source in the sky, that corresponds to the incoming direction of the emitted γ-ray.

4.4 DL2 to DL3

The following scripts are used to pass at **DL3** step, making data ready for the high-level analysis:

- `lstchain_create_dl3_file`
- `lstchain_create_dl3_index_files`

The first script creates DL3 files combining DL2 files with the corresponding IRF, the second script generates Header Data Unit (HDU) and Observations (Obs) tables. For a more sensitive analysis, for each run can be selected the IRF corresponding to the nearest node of the grid, referring to the grid point nearest to the telescope's pointing position in the sky.

It is possible to select this option adding the flag '–use-nearest-irf-node' during the creation of DL3 files, when the script is run in the correct environment that is provided with this option.

HDU table 'hdu-index.fits.gz' provides a list of all available HDUs:

- EVENTS: events list;
- GTI: Good Time Intervals, during which the data quality of the observations is considered acceptable for the analysis;
- POINTING: pointing directions of the telescope;
- AEFF: effective area;
- EDISP: energy dispersion;
- RAD MAX: radius of the directional cut applied to calculate the IRF.

The **Obs table** 'obs-index.fits.gz' file contains information about each observation, including:

- DATE-OBS: date of the observation;
- TSTART/TSTOP: starting and stopping time;
- RA-PNT/DEC-PNT: coordinates of telescope's pointing position;
- OBJECT: name of the observed source;
- OBS MODE: observation mode, the specific configuration and setup of the instrument during data acquisition.

It is important to update the index files every time a DL3 file is added, removed or modified.

4.4.1 Theta-squared distribution

A commonly used tool in γ-ray astronomy is the θ^2 **plot**, used to evaluate the quality of data and whether the observed events are consistent with the presence of a point-like γ-ray source. It can be performed using DL2 or DL3 files.

If events are concentrated near $\theta^2 = 0$ forming a clear and narrow peak, means that a signal from a γ-ray source is detected (see Fig. 4.4).

Theta-cuts are employed to reduce contamination from background events and focus the analysis on γ-ray events that are more likely to be associated with the source of interest. The choice of an appropriate theta-cut can be done by investigating the distribution of angular distances θ for the observed events and compare it to the expected distribution from MC simulations.

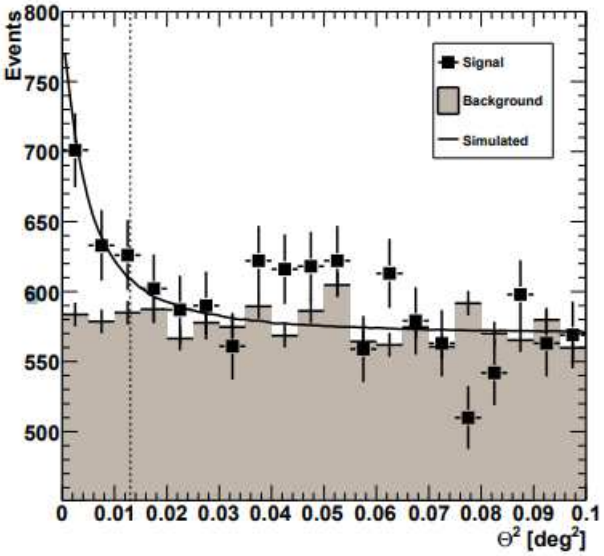

Figure 4.4: Example of a theta-squared distribution from VERITAS observations of 1ES 0806+524. The vertical dashed line indicates the size of the integration region. The solid line indicates the expected shape of the distribution for a point source. Both the detected signal counts and background are displayed [36].

The **significance** of the excess events above the background can be computed. A high significance value indicates that the observed excess is unlikely to be solely due to background fluctuations, suggesting the presence of a γ-ray source. In order to identify it, the significance should be above 5σ. The significance is calculated measuring the observed excess in the ON-region with respect to the background estimated from the OFF-region, taking into account the statistical fluctuations (see Formula4.2). In this analysis, the Li&Ma significance is calculated with the following formula [37], where the resulting value S_{LM} provides a measure of the

confidence level for the γ-ray detection:

$$S_{LM} = \sqrt{2}\left(N_{on} \cdot ln\left(\frac{(1+\alpha)N_{on}}{\alpha(N_{on}+N_{off})}\right) + N_{off} \cdot ln\left(\frac{(1+\alpha)N_{off}}{N_{on}+N_{off}}\right)\right)^{\frac{1}{2}} \tag{4.2}$$

4.5 High-level analysis

Once arrived at DL3 stage and selected γ-ray candidates, the analysis passes to the higher level with **Gammapy**, a Python package for gamma-ray astronomy built on *Numpy, Scipy* and *Astropy*. It provides tools to simulate the gamma-ray sky and analyse IACT data.

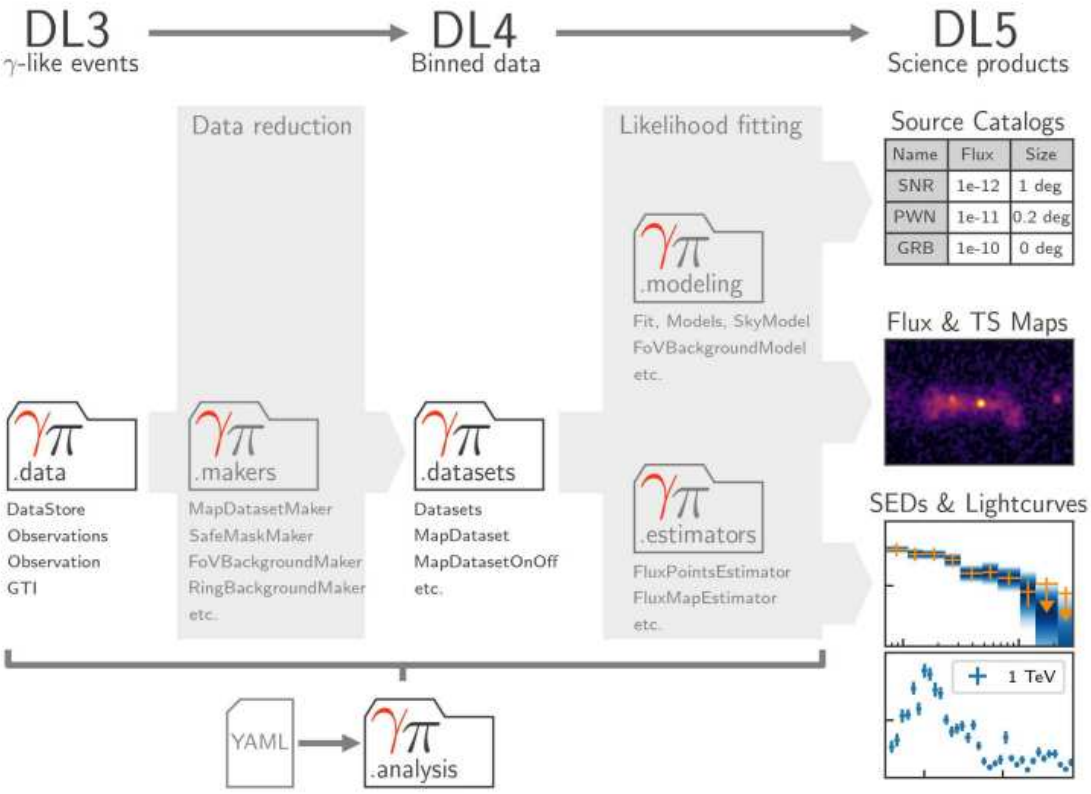

Figure 4.5: High-level analysis workflow with Gammapy [38].

Using Gammapy it is possible to obtain scientific results from calibrated data, extracting the **Spectral Energy Distribution (SED)**, **Light Curve (LC)** and **Sky Maps**.

4.5.1 Spectral energy distribution

The **spectral energy distribution (SED)** represents the flux emitted by a source as a function of energy and allows for the study of the emission properties. It is plotted with

$E^2 d\Phi(E)/dE$ on vertical axis and the energy (TeV) on the horizontal axis. $d\Phi(E)/dE$ is the **differential flux**, the energy flux per unit energy, typically defined in a given energy range $E_1 < E < E_2$ as:

$$\frac{d\Phi(E)}{dE} = \frac{N_{excess,E_1<E<E_2}}{t_{eff} \cdot A_{eff} \cdot (E_2 - E_1)} \tag{4.3}$$

where $N_{excess,E_1<E<E_2}$ is the number of excess in a given energy interval crossing a specific area A_{eff} in the effective observation time t_{eff} (calculated subtracting the *dead time* to the total observational time). Searching for the maximum value attained in the SED, where the emitted flux reaches the highest energy, is important for the investigation of dominant processes driving the VHE emission. The study of the SED is useful to understand how each wave-band contributes to the total emission. Usually, for a better investigation the total energy range is divided into discrete intervals or bins, allowing for a more accurate analysis of the spectral behaviour. The number and size of bins depend on the analysis requirements. An **higher number of energy bins** results in fine intervals, allowing for an increase of resolution and a better identification of features and variations. Fine energy bins help also to identify and characterize sharp features, such as spectral lines, peaks and cutoffs with higher precision. One of the disadvantage in having more energy intervals is that the number of data points in each bin decreases, leading to lower statistical significance and larger error bars.

On the other hand, with a **lower number of energy bins** the statistics is improved, since each bin contains a larger number of data points reducing uncertainties in measurements. This approach is useful if the dataset is limited, providing a more stable representation of the energy spectrum. Some disadvantages can be the loss of resolution and the reduction of sensitivity. The ability to distinguish between different emission components or spectral features may be reduced, resulting in lower sensitivity in the detection of distinct components of the spectrum.

4.5.2 Light curve

The **light curve (LC)** represents the time evolution of the integral flux above certain energy. The **integral flux**, defined in the energy range $E > E_0$, is:

$$\Phi(E > E_0) = \frac{N_{excess,E>E_0}}{t_{eff} \cdot A_{eff,E>E_0}} \tag{4.4}$$

where $N_{excess,E>E_0}$ is the number of photons above a certain energy E_0 crossing a specific area A_{eff} during the effective observation time t_{eff}.

The energy range has to be chosen carefully because if E_0 is close to the energy threshold (see Sec. 2.4) large systematic errors can be encountered.

As for the SED, the LC can be divided into **time bins**, with a variable number and size depending on the analysis requirements.

The choice of the time bin size in the LC is influenced by two important variables: the number of detected photons and the duration of the observation. If the dataset covers a time range of months or years, larger time bins of several days may be suitable. On the other hand, if the dataset covers a shorter time interval of days, time bins can be reduced to hours or even minutes. The objective is to find a balance between having enough photons for statistical significance and preserving the ability to identify temporal variations of the source.

Smaller time bins provide higher time resolution allowing for a more precise characterization of physical processes governing the emission. This binning can reveal rapid changes in the source, helping to identify specific features like flares or periodic oscillations. However, this approach might leads to lower statistical significance due to limited photon counts in each bin, resulting in the risk of overfitting data, meaning they can become too sensitive to noise.

Larger time bins can improve the statistical significance of the analysis, reducing noise and fluctuations. They can help to identify long-term patterns in the dataset, which might be masked by short-term variations. Nevertheless, this approach reduces the temporal resolution and the accuracy for studying the short-variability of the source, therefore it is not particularly suitable for transient phenomena.

According to these considerations, it can be deduced that is more reasonable to observe a source that is in an *high-state* of emission. This means that the source is emitting γ-rays at a significantly elevated rate compared to its usual emission level.

4.5.3 Sky maps

Skymaps are 2D images that represent the distribution of selected γ-ray candidate events in the sky. They provide a spatial representation of the observed or predicted γ-ray emission, allowing to study the spatial distribution of sources. These histograms are created firstly constructing an OFF background map from a camera exposure model that takes into account inhomogeneities of the camera. Then, data from events are utilized to generate an ON map. Skymaps are useful for source detection, localization and morphological studies.

Gammapy provides tools to obtain these outcomes, after transforming data into flux points with the **FluxPointsEstimator**. The **LightCurveEstimator** is used to build the light curve; the **Map** tool creates a **MapAxis** object, that internally stores the coordinates or "position values" associated with every map axis bin, and it is utilized to create Skymaps.

Moreover, Gammapy includes **temporal, spectral and spatial model** classes. All models are built on default parameters, that can be changed in the command lines when the model is defined.

Chapter 5

PG 1553+113 analysis with LST-1 data from 2021 to 2023

In this chapter is described the LST analysis I performed of PG 1553+113 from 2021 to 2023, corresponding to when LST-1 started to take PG 1553+113 data up to the latest available observations. Multi-wavelength data from X-rays and HE bands are also shown in Section 5.1. All the analysis steps are described in detail in the next sections, selection masks on parameters are specified and some illustrative plots are presented.

5.1 Multi-band comparison

In this section, LST-1 data are contextualized with data taken by **Fermi-LAT** in the HE band and **Swift-XRT** in X-ray band during the years.

Fermi is a space observatory focused on detecting γ-rays in the energy range from $\sim$20 MeV to $\sim$300 GeV. It is equipped with two main instruments: the **Large Area Telescope (LAT)** and the **Gamma-ray Burst Monitor (GBM)**. The LAT is a high-resolution imaging detector that can point γ-ray sources with energies from $\sim$20 MeV to $\sim$300 GeV, instead the GBM is designed to detect transient events from few keV to $\sim$40 MeV.
Swift is also a space observatory, equipped with three main instruments: the **Burst Alert Telescope (BAT)** for detecting GRBs operating in the hard X-ray and soft γ-ray energy range ($\sim$15 keV to $\sim$150 keV); the **X-ray Telescope (XRT)** covering the X-ray energy range from $\sim$0.2 keV to $\sim$10 keV; the **Ultraviolet/Optical Telescope (UVOT)** that operates in the ultraviolet and optical bands.

Data of PG 1553+113 by *Swift-XRT* (May 2005 - July 2023) are in Figure 5.1, while *Fermi-LAT* observations (August 2008 - July 2023) are shown in Figure 5.2, in which is indicated the time interval corresponding to the LST-1 dateset (March 2021 - April 2023).

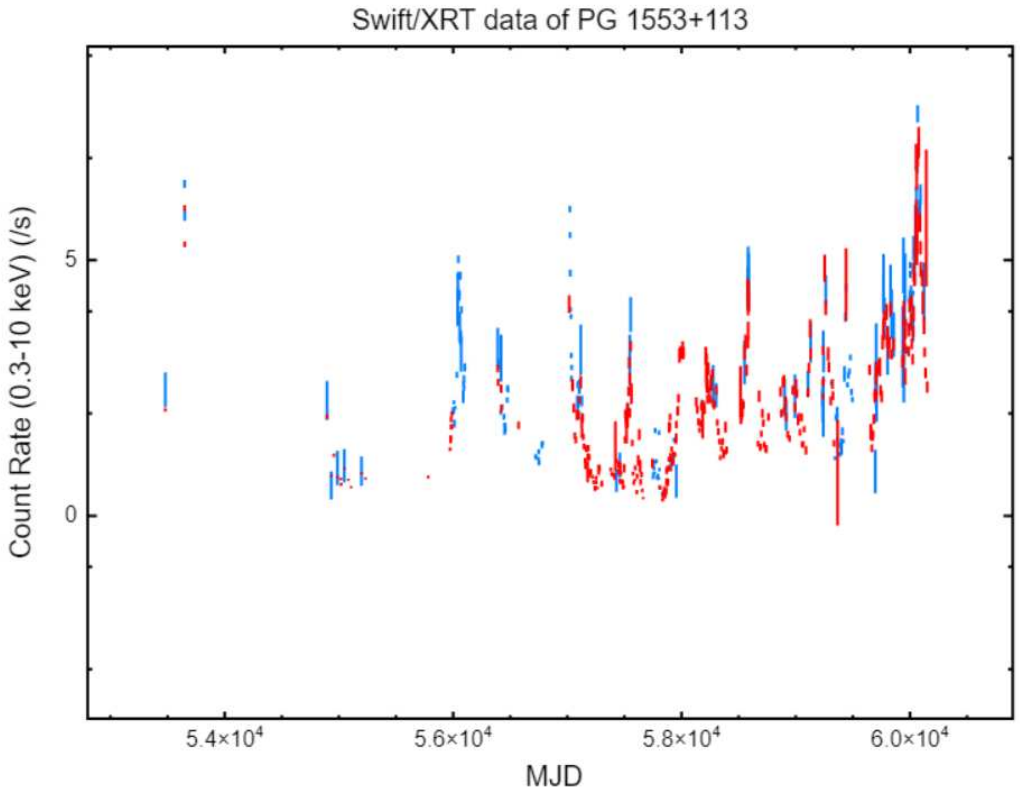

Figure 5.1: Swift-XRT data of PG 1553+113 from May 4th 2005 to July 27th 2023. The LC is binned to one bin per observation. Here is represented the count rate as a function of time in MJD. (LC taken from the Swift website: *https://www.swift.ac.uk/user_objects/*)

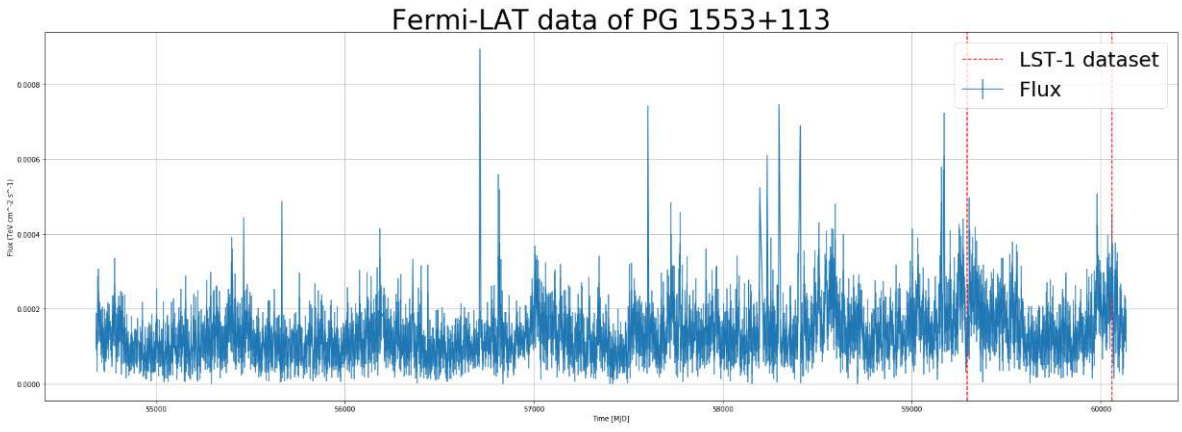

Figure 5.2: Fermi-LAT observations (above 100 MeV) from August 6th 2008 to July 23th 2023. The flux is plotted as a function of time in MJD. The observation period corresponding to the LST-1 dataset is denoted in red and goes from 59294 to 60059 MJD. (Data taken from *https://fermi.gsfc.nasa.gov/ssc/data/access/lat/LightCurveRepository/*)

Fermi-LAT performed a continuous monitoring on PG 1553+113, revealing a **quasi-periodic emission in the HE** γ-ray band of 2.18 ± 0.08 years [39]. It can be seen in Figure 5.2, where flux peaks can be recognized in the light curve, arising approximately every two years. This is the **first time** such a periodicity has been found convincingly in a γ-ray blazar.
Swift-XRT, on the contrary, **does not show** evidence for a significant periodicity or intra-day variability [16]. Instead, in the X-band an **intra-day variability** of 2.4 ± 0.7 kiloseconds (corresponding to approximately 0.67 hours) was recently found in the energy range 0.3 – 10 keV from data collected by *XMM-Newton* [40].

The light curve extraction performed with LST-1 data of PG 1553+113 in this thesis allows a comprehensive multi-band comparison, extending the available energy ranges to the VHE domain. This provides an opportunity for a more exhaustive cross-comparisons, facilitating the identification of potential trends or deviations that might have been previously missed.

5.2 Data reduction

Starting from DL1 files, a selection of observations from March 2021 to April 2023 is performed, in order to identify runs with favorable observational conditions. After finding runs in which the telescope was pointing toward the source of interest, **several cuts** are applied to achieve different purposes:

- a cut to esclude runs with **issues on pedestals** (the electronic signal readings obtained from a detector when there is no input);
- a cut on the **angular distance** to select observations in a range between **0.35 deg** < θ < **0.45 deg** from the source and exclude regions of the sky where there might be significant background contributions;
- a cut on the zenith angle selecting **0 < zenith < 52 deg**, to limit the background contribution that can be higher near the horizon;
- the **Sun position** at observation time is checked to esclude twilight data and ensure that the Sun is always below the horizon;
- a cut for checking the **average pixel rate of photoelectrons pulses** in cosmics: low rates may indicate poor weather or telescope problems, high rates might be due to car flashes, satellites etc.;
- a cut on **flatfield events standard deviation**, useful to calibrate the detector response and correct for any non-uniformities of the detector. A flatfield event is a type of cali-

```
1 : 2021-03-21 : [4207]
2 : 2021-04-07 : [4333, 4334, 4335, 4336]
3 : 2021-04-08 : [4343, 4344]
4 : 2021-04-10 : [4363, 4364, 4365, 4366, 4367, 4368]
5 : 2021-04-20 : [4514, 4515]
6 : 2021-05-08 : [4652, 4653, 4654]
7 : 2021-06-04 : [4902, 4903, 4904, 4905]
8 : 2021-06-05 : [4930, 4931, 4932]
9 : 2021-06-06 : [4940, 4941, 4942, 4943]
10 : 2022-02-28 : [7153, 7154]
11 : 2022-05-01 : [8059, 8060, 8061, 8062, 8063, 8064]
12 : 2022-05-20 : [8377, 8378]
13 : 2022-05-23 : [8424, 8425]
14 : 2023-01-20 : [11749, 11751]
15 : 2023-01-23 : [11809, 11810, 11811, 11812]
16 : 2023-01-26 : [11903, 11904, 11906]
17 : 2023-02-24 : [12080, 12081, 12082, 12083, 12084, 12085]
18 : 2023-02-26 : [12096, 12097, 12098]
19 : 2023-03-17 : [12234, 12235, 12236, 12237]
20 : 2023-03-21 : [12362, 12363, 12364, 12365, 12366]
21 : 2023-03-29 : [12544, 12545]
22 : 2023-04-14 : [12697, 12698, 12699, 12700]
23 : 2023-04-18 : [12755, 12756, 12757, 12758]
24 : 2023-04-25 : [12859, 12864, 12865, 12866, 12867, 12868, 12869, 12870, 12871, 12872, 12873, 12874]
```

Figure 5.3: List of selected runs with the respective observation date.

bration event that involves observing a uniform light source or an empty region of sky in order to measure the response of the telescope to a uniform light distribution. A lower flatfield event standard deviation indicates that the detector is responding more uniformly across the field of view.

At the end, the result is a list of optimal runs to proceed with the analysis: **90 runs** for an observation time of **24.84 hours**, from **21-03-2021** to **25-04-2023**.

Those selected files must be transformed in **DL2 files**. RF models developed for the *declination 9.31 deg* are applied, the closest one to that of the source.

At this point, **IRF files** must be created, using MC simulations performed for declination 9.31 deg for all the nodes of the grid and a configuration file containing details on "EventSelector", "DL3Cuts" and "DataBinning".

- **"EventSelector":** filters on the intensity, width and lenght of the signal, to select events with Hillas parameters (Fig. 4.1) in a given range. Having a minimum intensity is to ensure a certain photon statistic in the image, while filters on the shape of the signal are to select the most likely γ-ray like events.

- **"DL3Cuts":** set the minimum and maximum value of the γ/hadron efficiency and of the θ value, indicate the minimum number of events per energy bin.

- **"DataBinning":** information about the binning of the true, reconstructed and migration energies, and also about the offsets of the FoV, background and source.

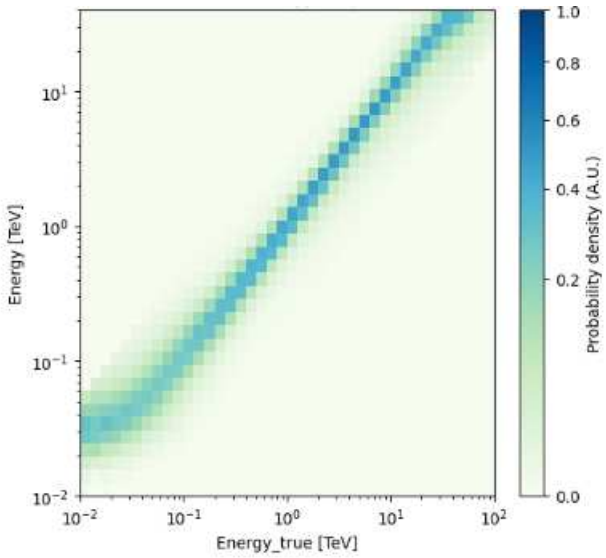

Figure 5.4: The energy migration matrix, a two-dimensional matrix where each element (i, j) indicates the probability that a γ-ray photon of true energy in bin i will be detected in energy bin j.

The relationship between the true and reconstructed energy values is represented with the **energy migration matrix** (also known as the *response matrix* or *energy dispersion matrix*) shown in Figure 5.4, built by comparing the true energy of MC simulated photons to their corresponding reconstructed energy obtained from the data analysis. The probability density represents the likelihood of a γ-ray photon originating from a certain energy range being detected in another energy range.

IRFs are created specifying in the appropriate script the following flags:

- `–point-like`, IRFs for point-like sources;
- `–energy-dependent-gh`, an energy dependent γ/hadron separation;
- `–energy-dependent-theta`, an energy dependent θ, the angular distance between the reconstructed arrival directions of the events and the source nominal position;
- `–gh-efficiency=0.95`, required efficiency (95%) for the γ/hadron separation;
- `–theta-containment=0.68`, the fraction (68%) of the area where the distribution of recorded events is concentrated.

These IRFs are combined with DL2 files to create **DL3 data**. To use the IRF's nearest node for each run, there are two ways to proceed:

1- using the appropriate flag in the script for the creation of DL3 files in the correct updated enviroment;

2- running a script available for the LST collaboration, that provides the list of each observation ID with the corresponding nearest node. Then insert a loop inside the script for creating DL3 files to select every time the right node.

Both methods were tested, then data generated using the first approach are selected to proceed with the analysis. Some information contained into DL3 fits files are shown in Figure 5.5, where there are represented the source's position in the sky in the galactic frame, number of counts at a given offset, counts as a function of increasing energy and of time.

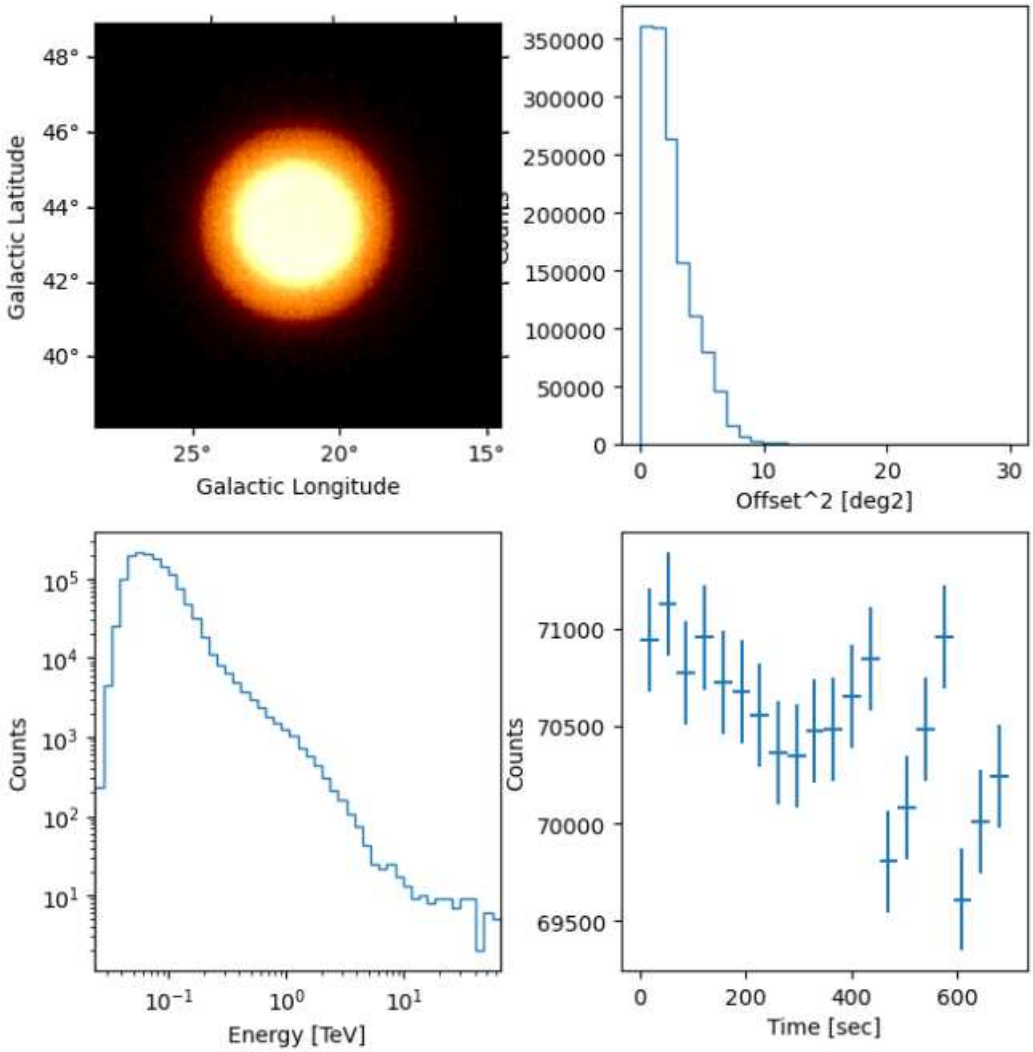

Figure 5.5: Information stored in the DL3 file of the Run 12874: distribution of the telescope pointing direction, counts as a functions of offset, energy and time. As expected, counts decrease with increasing energy.

Gammapy tools can be now applied to the calibrated dataset, after defining the energy binning and derived some quantities used for the high-level data analysis.

5.2.1 High-level analysis setup

The **energy binning** is "per decade", meaning that the energy range is divided into equal intervals in logarithmic units. It is possible to choose a different binning for the reconstructed and true energy. Typically, the number of bins per decade of the **true energy** is very high, in order to have a more precise and detailed description of the energy distribution, using a fine-grained binning over the wide range of emitted energy.

The **reconstructed energy** is setted to a minimum value of 10 GeV and a maximum of 40 TeV. The **true energy** is fixed to a minimum of 10 GeV and a maximum of 100 TeV, and the interval is divided into 10 energy bins.

A fundamental step is also the definition of the **energy threshold**. This value is estimated from the merged files of MC simulations available for all nodes. The value of the threshold is represented by the peak of the energy distribution and it is equal to 33.70 GeV, approximated in the analysis to 35 GeV.

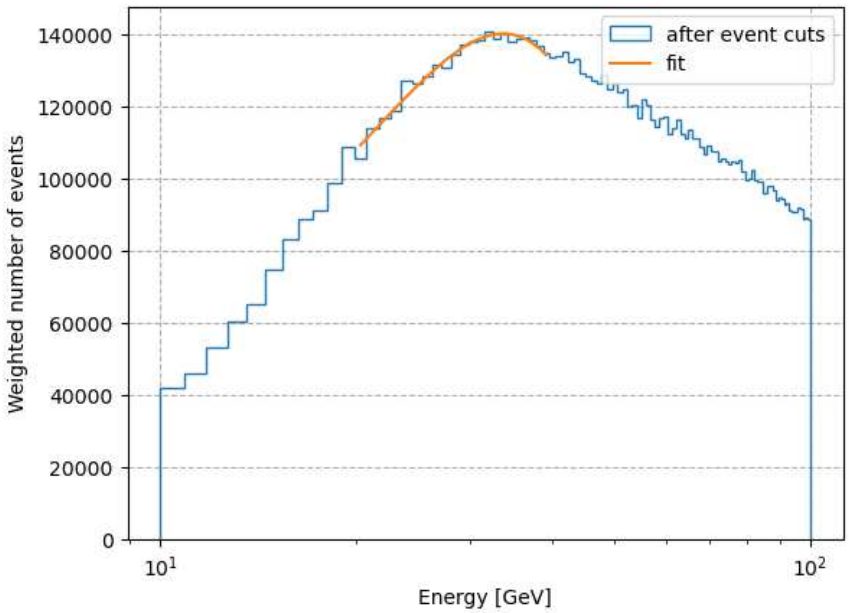

Figure 5.6: The energy threshold of LST-1 used to perform MC simulations. The weighted number of events is fitted with a Gaussian. The value at the peak is equal to E=33.70 GeV.

5.2.2 Map geometries

A **'MapAxis'** can be created, defining the boundaries of energy values over which the γ-ray emission is measured. A 'MapAxis' is a class of objects used to discretize into bins a quantity like the energy instead of treating it as a continuous variable. Each bin represents a range of energy, making the analysis simpler and more manageable. 'MapAxis' objects are

often used together with other classes in Gammapy to work with multi-dimensional data, such as 'Map' or 'DataStore'.

'Map' geometries provide the spatial context necessary for analyzing and interpreting the collected data. They represent the distribution of events, background estimations, or other relevant quantitiesm and are represented in Figure 5.7.

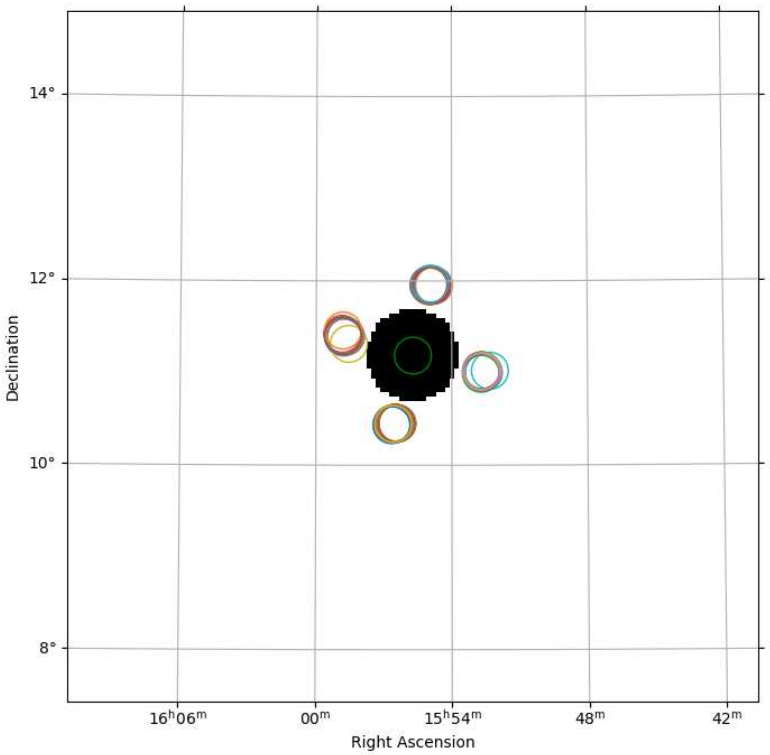

Figure 5.7: In the plot are represented: the ON region (the green circle in the centre); the 4 OFF regions used for the calculation of the background; the exclusion mask in black with radius 0.5 deg.

'Map' geometries that are defined are:

- **ON region:** a region centered on the source position, with an ON radius equal to **0.2 deg**, to limit the background contribution and select only the source region. It's geometry is defined by the **ON geometry**, a 'Map' that refers to the spatial configuration indicating the shape, size, position and other additional paramters used to define the ON region;
- **OFF regions:** regions with the same size of the ON region, in correspondence with the wobble positions. They are used for the calculation of the backgorund.
- **Exclusion Region:** region centered on the source position with a radius of **0.5 deg**, to be excluded during the creation of the background. It's usually identified to avoid source contamination during the estimation of the background.

5.2.3 Dataset

The background is created using the reflected-regions technique (see Sec. 3.2.3) with the **'ReflectedRegionsBackgroundMaker'**.

Estimating the background before forming the dataset ensures that the background is properly characterized. This allows to subtract it from the observed counts to get the excess counts associated to the source.

The dataset typically contains observed counts in each direction and energy bin, combined with other information like time of observations, exposure (how much of the sky was observed at different energies), energy dispersion and significance, indicated as square root of the test statistic. The excess, exposure and energy migration matrix are shown in Figure 5.8, while the evolution of the significance as a function of time is represented in Figure 5.9. The increasing trend suggests that the observed signal becomes more distinct from the expected background-only scenario as more data are accumulated, resulting in a higher statistical significance.

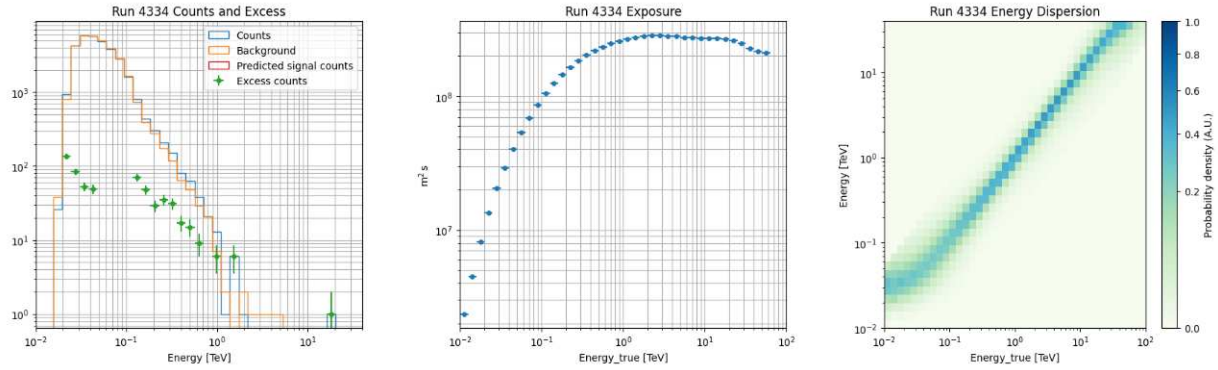

Figure 5.8: Run 4334. (*Right*) Counts and background computed for each energy bin, from which the excess are obtained with related uncertainties. The predicted signal has not been computed. (*Middle*) Exposure related to the true energy. (*Right*) Energy migration matrix.

The spectrum dataset is created with the **'SpectrumDatasetMaker'**, making use of a safe mask for the energy. This **safe mask** represents the energy range within which the data can be considered reliable and accurate for analysis. Here is setted between 50 GeV and 20 TeV, . It is generated with the **'SafeMaskMaker'** and used during the creation of the spectrum dataset.

The proposed approach is to use a **stacked dataset**, obtained from the combination of multiple observations into a single dataset. This method is useful to increase the statistical power and improve the sensitivity of the analysis.

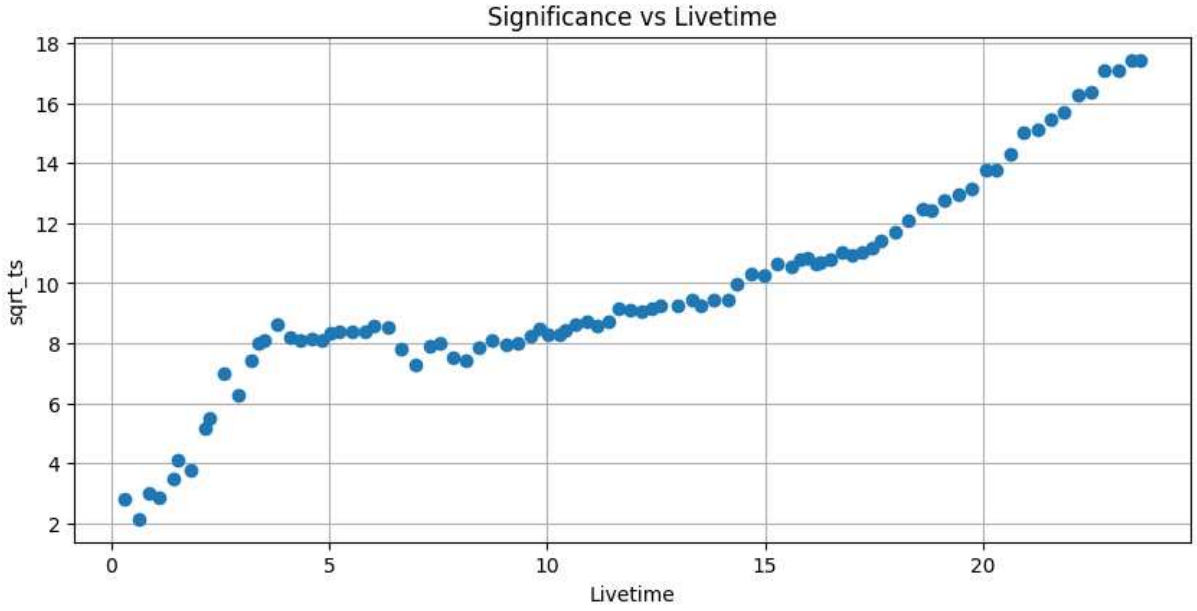

Figure 5.9: Evolution of the significance as a function of livetime. It increases as expected, as more photons from the source are collected over time and the statistical uncertainty in the measurement decreases.

5.2.4 Spectral models

Spectral models available in Gammapy are listed below:

```
ConstantSpectralModel
CompoundSpectralModel
PowerLawSpectralModel
PowerLaw2SpectralModel
BrokenPowerLawSpectralModel
SmoothBrokenPowerLawSpectralModel
PiecewiseNormSpectralModel
ExpCutoffPowerLawSpectralModel
ExpCutoffPowerLaw3FGLSpectralModel
SuperExpCutoffPowerLaw3FGLSpectralModel
SuperExpCutoffPowerLaw4FGLSpectralModel
LogParabolaSpectralModel
TemplateSpectralModel
GaussianSpectralModel
EBLAbsorptionNormSpectralModel
NaimaSpectralModel
ScaleSpectralModel
PowerLawNormSpectralModel
LogParabolaNormSpectralModel
ExpCutoffPowerLawNormSpectralModel
```

Figure 5.10: List of available spectral models in Gammapy.

To describe the spectral shape of data, a **'PowerLawSpectralModel** is created and combined with an **'EBLAbsorptionNormSpectralModel'**. The **power-law** spectral model is

described by the equation 5.1:

$$\Phi(E) = \Phi_0(\frac{E}{E_0})^{-\Gamma} \tag{5.1}$$

where $\Phi(E)$ is the flux of γ-ray photons at energy E and Φ_0 is the amplitude that determines the overall scaling or normalization of the spectrum. E_0 is the reference energy, that corresponds to the decorrelation energy, the value below which the response of the instrument is uncorrelated with the true photon spectrum. Γ is the spectral index that governs the shape of the spectrum. It indicates how quickly the flux decreases with increasing energy. A smaller index value results in a steeper spectrum, a more rapid decrease with energy. The **EBL** spectral model is used to correct the spectrum for the absoption which affects the VHE domain. It is described by the following formula:

$$e^{-\alpha \cdot \tau(E,z)} \tag{5.2}$$

where $\tau(E, z)$ is the optical depth predicted by the model, which depends on the energy of the γ-rays and the redshift z of the source (z=0.433), and α is a scale factor for the optical depth, setted by default to 1. In this analysis, is applied the **Dominguez model** for EBL.

After fitted the model, flux points can be computed using the **'FluxPointsEstimator'**. This tool estimates also asymmetric errors on flux, upper limits and fit statistic profiles.

5.3 Results

In this section are illustrated the results obtained from the analysis of the dataset: the θ^2 distribution in Sec. 5.3.1, the light curve in Sec. 5.3.2, the spectrum and spectral energy distribution in Sec. 5.3.3.

5.3.1 Theta-squared distribution

The θ^2 distribution is calculated for the stacked dataset within the energy range between 10 GeV and 1 TeV, considering a cumulative exposure time of 23.53 hours. A cut at θ^2= 0.04 degrees (θ= 0.2) is applied to data, to reduce contamination from background events. The total significance stands at **23.17** σ, indicating the **detection of a γ-ray signal** from the source. Figure 5.11 displays the signal counts, providing a visual comparison against the background. The increase in the source signal below 0.04 degrees is due to the presence of a γ-ray source. Consequently, the signal reaches its **maximum intensity** at θ^2=0, representing the direct alignment with the source's position. On the other hand, the gradual increase in background counts as θ^2 increases can be attributed to the instrument's field of view and the way background events are distributed across the sky. As θ^2 moves away from the source position, the

instrument's field of view covers a larger portion of the sky, including regions where background events are more prominent, and the PSF becomes broader. Therefore, the probability of capturing background events also increases, leading to a rise in the background counts.

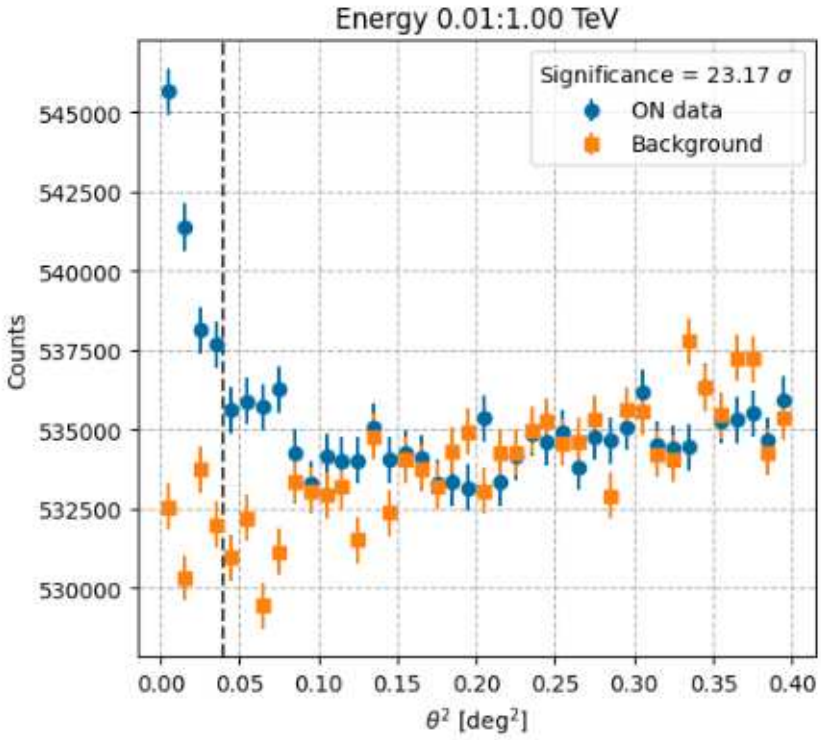

Figure 5.11: Theta-squared distribution for the whole dataset (Runs 4333:12874), for a total observation time of 23.53 hours, in the energy range between 10 GeV and 1 TeV. The dashed line represents the location of the cut θ^2 = 0.04 applied to data. The cut retains events which lie to the left of the line.

5.3.2 Light Curve

To compute the light curve, from each observation are extracted the Good Time Intervals (GTI). Light curve points for each run and for each night are estimated by the **'LightCurveEstimator'**, to produce **run-wise** and **night-wise** binned light curves. For each of these points, the flux and significance are estimated, together with other useful parameters.

During the construction of the LC, a **threshold on the significance** is applied, determining whether a point should be considered as a standard data point or as an upper limit. In this analysis, the significance threshold is setted to $\mathbf{2}\sigma$. If a data point exceeds this specific value, it is represented as a regular light curve point. However, if its significance is not sufficiently high, it transforms into an **upper limit** and is indicated with a downward arrow, as showed in Figure 5.12.

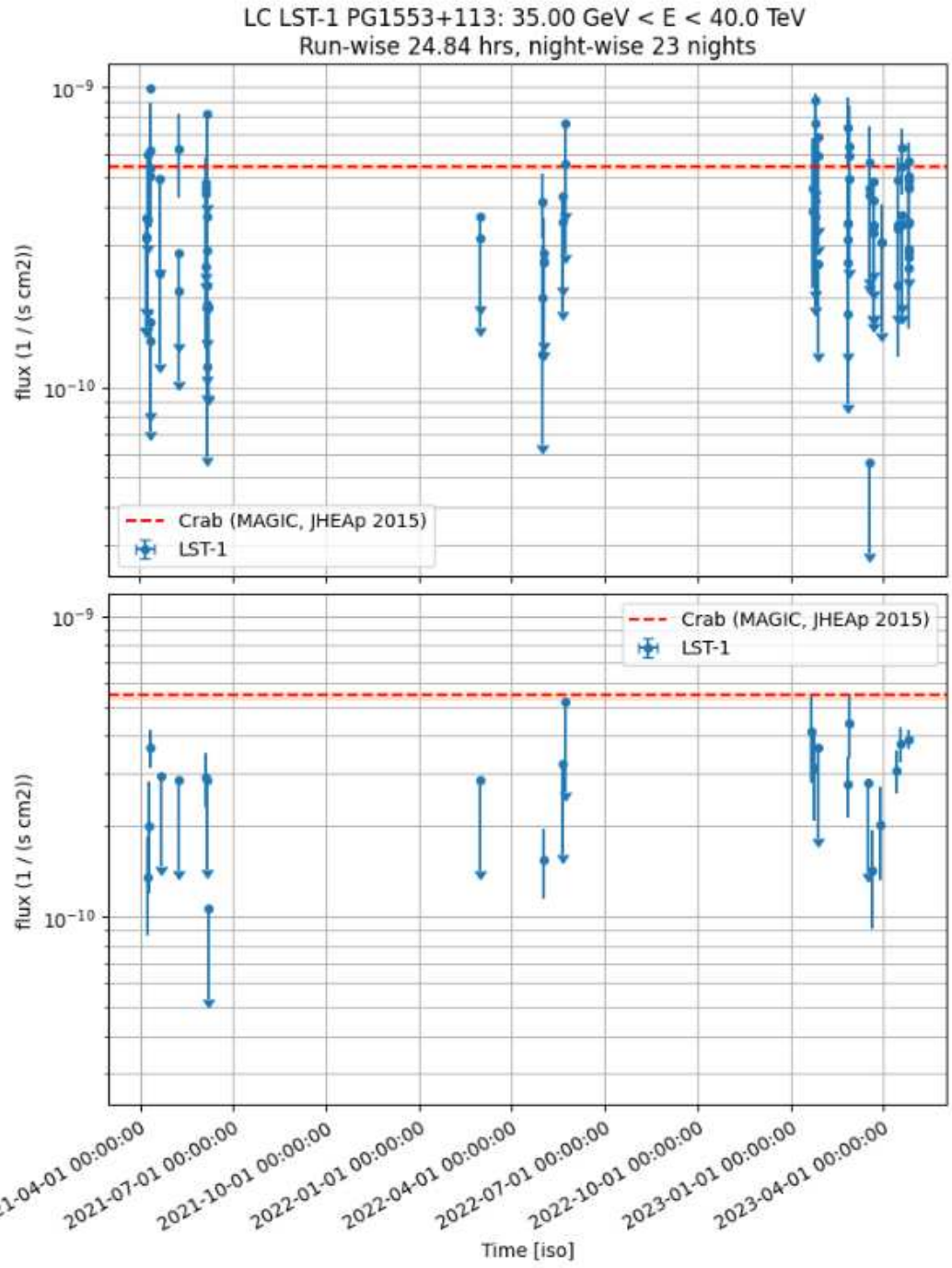

Figure 5.12: (*Top*) Run-wise light curve for a total time of 24.84 hours. Each point represents a different run. (*Bottom*) Night-wise light curve for 23 nights. Each point represents a different night. The Crab's flux in red is used as a refrence flux. The energy threshold is setted to 35 GeV.

It is noticeable to observe the variation in the number of upper limit points between the run-wise and night-wise light curves. The run-wise exhibits a higher number of upper limits, and this is attributed to the reduction of the time binning. Reducing the binning, the significance for each bin decreases since fewer counts contribute to each individual point, leading to a higher number of upper limits compared to the light curve with larger bins.

Analyse a dataset that covers a relatively large time interval is useful to identify and characterize **periodic components** in the light curves. Recurring patterns or periodic signals may indicate the presence of underlying periodic processes, such as orbital motion, precession or intrinsic changes in the emission region. This kind of study helps to identify a periodic behaviour of the source, and it is what has been done by investigating the features in the light curve in HE band, which have been attributed to the dynamics of a system of two SMBHs [17].

An additional test is performed to evaluate how much the flux emitted by PG 1553+113 deviates from a steady behavior. In order to do this, the night-wise light curve is fitted with a **constant flux**, as shown in Figure 5.13. The deviation is quantified by the residuals, which refer to the difference between the observed and the expected values (in this case, the constant ones). They are used to assess the goodness of fit of a statistical model to the observed data. If the residuals are small and evenly distributed around zero, it suggests that the model is a good fit to the data. From the plot 5.13, it can be observed that the points significantly deviate from zero, suggesting that a constant flux **does not appropriately describe** the emission of the source, as expected for a blazar, characterized by a variable emission (see Chapter 1.1).

A statistical procedure for comparing observed and expected data is applied: a **chi-square (χ^2) test**. The goal of this test is to identify whether a disparity between actual and predicted data is due to chance or to a link between the variables under consideration. The χ^2 is a weighted sum of squared deviations, calculated using the following equation:

$$\chi^2 = \sum \frac{(O_i - E_i)^2}{\sigma_i^2} \tag{5.3}$$

where O_i are the observed data, E_i are the expected ones, and σ_i is the error associated to each observed point.

This value is calculated to obtain the **reduced chi-square (χ^2_{red})**. It is a revised version of the standard χ^2 statistic, which takes into account the degrees of freedom (ν) in the data and model. The degrees of freedom are the number of independent data points from which are subtracted the number of parameters being estimated in the model. In the case of a constant flux, the number of parameters is equal to 1. The χ^2_{red} is defined as in the equation 5.4:

$$\chi^2_{red} = \frac{\chi^2}{\nu} \tag{5.4}$$

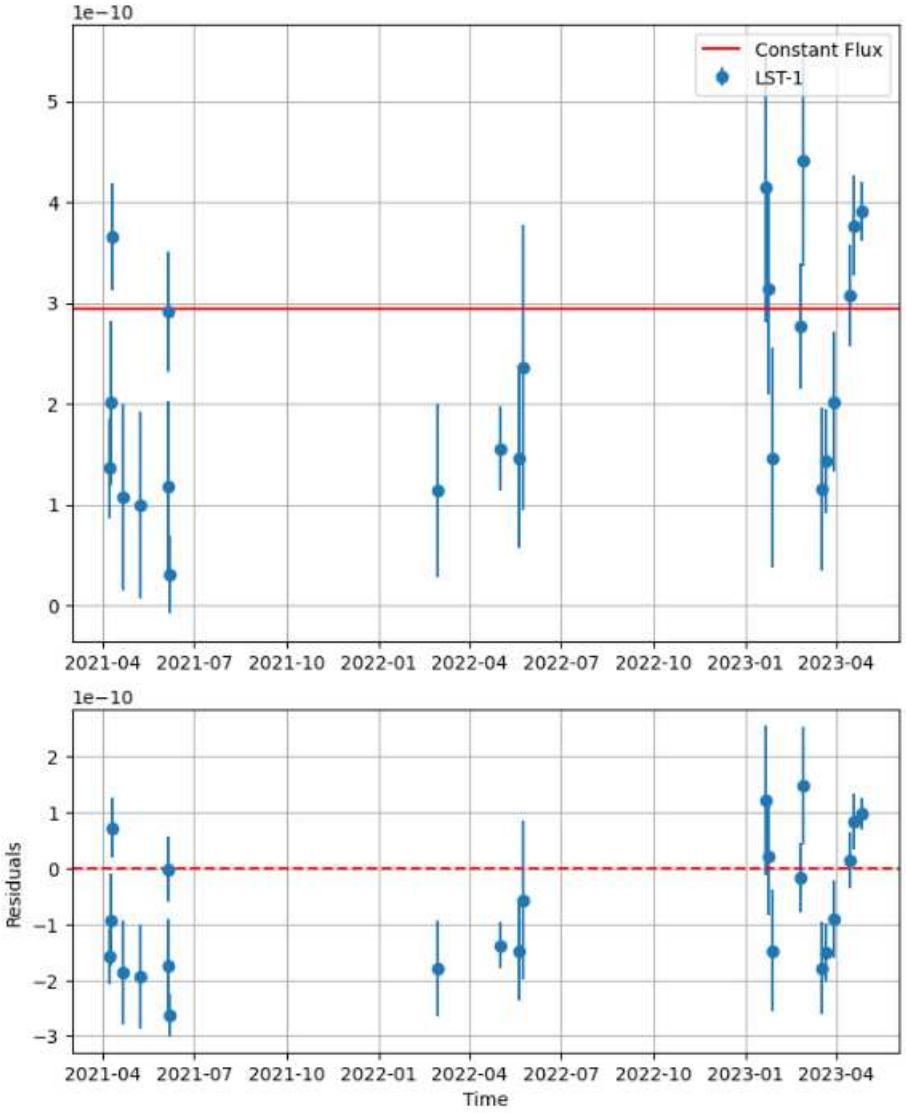

Figure 5.13: The night-wise light curve fitted with a constant flux and the corresponding residuals in the bottom panel.

A value $\chi^2_{red} \sim 1$ means that the model provides a good fit to the data, with the expected variation between observed and expected values. The condition $\chi^2_{red} \gg 1$ implies an inadequate fit of the model, suggesting significant discrepancies.

Based on the statistical analysis conducted on the data, the values of the χ^2 and χ^2_{red} are:

$$\begin{aligned} \chi^2 &= 127.00793003829334 \\ \chi^2_{red} &= 5.773087729013334 \end{aligned} \tag{5.5}$$

meaning that the hypotesis of a constant emission is not appropriate to describe the radiation emitted by PG 1553+113.

5.3.3 Spectrum and energy distribution

The **differential spectrum** is computed for the whole dataset and showed in Figure 5.14. A differential spectrum is a representation of how the differential flux changes as a function of energy. Here the flux points are fitted with a Power Law + EBL (Dominguez) model, to take into account the decrease in flux with increasing energy due to EBL absorption, that affects the VHE domain. Then, the **deabsorbed flux** is computed and shown in Figure 5.14. In the Figure there are some upper limits, indicated with an arrow. This occurs when the observed number of photons in a particular energy bin is too small to provide a statistically significant measurement of the flux, but it is still possible to set an upper limit on the expected flux. The detected flux points are from 40 GeV to 400 GeV, approximately.

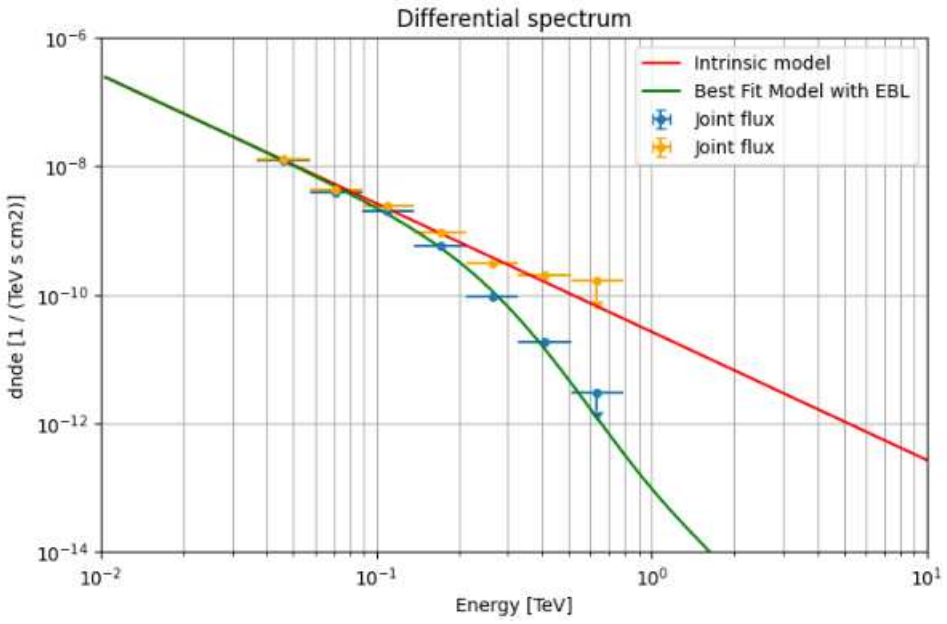

Figure 5.14: Differential spectrum of PG 1553+113 fitted with a Power Law + EBL (Dominguez) spectral model in *green*, intrinsic spectrum in *red*, without the EBL.

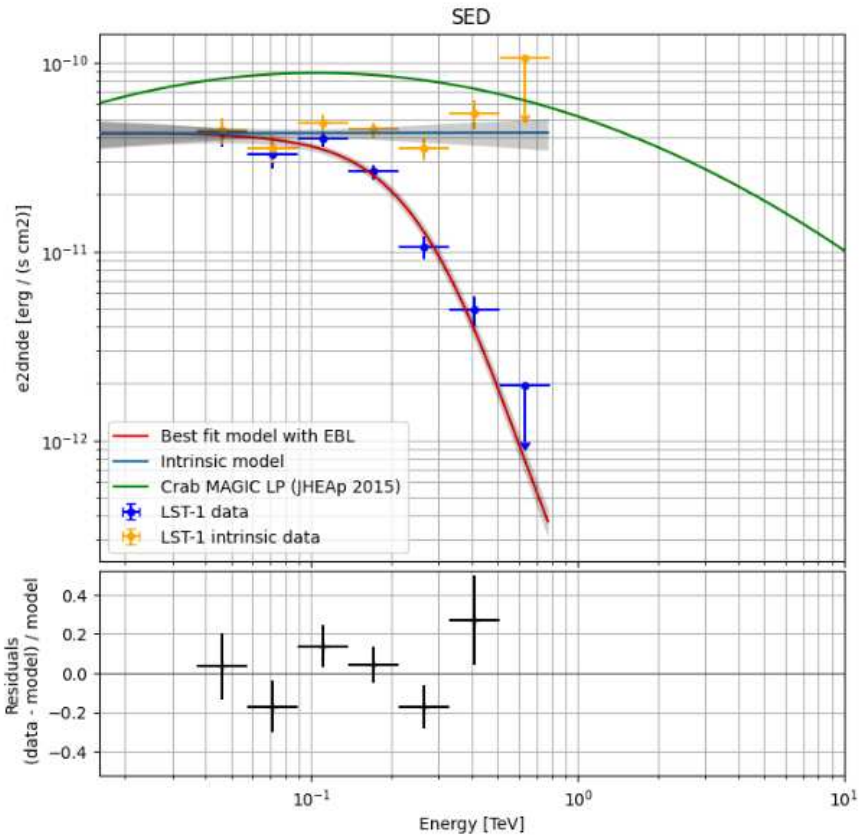

Figure 5.15: (*Top*) SED from LST-1 data of two years observations of PG 1553+113. Both observed and intrisic flux are represented. The grey region is the range of values that could be considered compatible with the measured data. (*Bottom*) SED residuals plot corresponding to the observed flux points.

Another achieved result is the **SED** of observed and intrinsic flux represented in Figure 5.15. It is calculated dividing the reconstructed energy range in 5 energy bins, while the binning of the true energy is setted to 100. Observed flux points are fitted with a Power Law + EBL (Dominguez) model. The covered energy range goes from ∼40 GeV to 400 GeV. From the plot, it is noticeable that the observed SED in the VHE range corresponds to the region just following the second peak of the typical blazar SED, which usually falls in the HE range.
The fact that the intrinsic flux appears to exhibit a 'flat' behaviour, resulting in a reduced visibility of the inverse Compton peak, could be attributed to the presence of data that reflect the source's variable emission. In the dataset, it is possible to have observations where the second peak of the SED occurs at lower energies compared to other observations where it is found at higher energies. Collecting these significantly varied values contributes to the observed spectral profile. The location of the SED peak, where the emitted radiation reaches its maximum intensity, is important for studying the particle acceleration and dominant emission mechanisms occurring in blazars.

Chapter 6

PG 1553+113 analysis of intra-night variability

This chapter is focused on the analysis of a single night, the one between April 25th and 26th 2023, during which a deep observation of PG 1553+113 lasting 4 hours was conducted by LST-1. The request for this deep observation derived from intention to investigate intra-night variability in the VHE range, following the detection of the intra-day variability observed by *XMM-Newton* (see 5.1).

Cherenkov observations are well-suited for studying **intra-night variability** due to the characteristics of Cherenkov telescopes: the **large effective area**, that enables for the detection of relatively low flux levels and the possibility to perform **uninterrupted observations** over several hours to capture and analyze flux changes occurring within a single night.

LST-1 is particularly suitable for this purpose, as it is more sensitive to lower energies ($\sim$20 to $\sim$150 GeV). Observing at **lower energies** allows to monitor the intra-night variability of the source more effectively. This is primarily because observations conducted at lower energies yield significantly **higher counts**, providing a notably enhanced sensitivity. This is attributed to a more accurate error estimation, coupled with a substantially larger amount of data available for statistical analysis. A large number of counts enables the construction of a proper light curve to investigate more thoroughly the temporal behavior of the source.

The aim is to detect and characterize rapid changes in the γ-ray flux on **timescales of hours to minutes**, associated to changes in the jet dynamics or interactions with the surrounding environment.

The variability at those timescales suggests a very compact emission and can be used to set an **upper limit** on the **minimum size of the emission region** in the jet, given by [41]:

$$R \leq \frac{\tau c \delta}{1+z} \tag{6.1}$$

where δ is the Doppler factor, z is the reshift and τ is the variability timescale. A minor vari-

ability corresponds to a smaller region located in **closer proximity** to the central black hole. From the timescale variability found with *XMM-Newton*, referring to the Formula 6.1, it can be obtained that the size of the emission region is in the range of $0.55 - 1.76 \cdot 10^{15}$ cm.

In the following section is the described the data reduction (Sec. 6.1), then are highlighted the results of the analysis, such as the theta-squared distribution (Sec. 6.2.1), light curve (Sec. 6.2.3) and spectra (Sec. 6.2.2).

6.1 Data reduction

The same data reduction methods as before are employed, although a different approach in the study of the light curve is utilized. This difference is due to the specific circumstances of all observations being from the same night, with the objective of detecting potential variability.

The energy configurations, geometries, spectral models and assumptions are exactly the same as the previous Chapter 5.2.

The dataset which includes **observations from 2023** is composed by 49 runs, for a total observational time of **13.182 hours**. Among these observations, **3.72 hours** are specifically from the night between April 25th and 26th. Runs that belong to the 2023 dataset are displayed in Fig. 6.1.

```
2023-01-20 : [11749, 11751]
2023-01-23 : [11809, 11810, 11811, 11812]
2023-01-26 : [11903, 11904, 11906]
2023-02-24 : [12080, 12081, 12082, 12083, 12084, 12085]
2023-02-26 : [12096, 12097, 12098]
2023-03-17 : [12234, 12235, 12236, 12237]
2023-03-21 : [12362, 12363, 12364, 12365, 12366]
2023-03-29 : [12544, 12545]
2023-04-14 : [12697, 12698, 12699, 12700]
2023-04-18 : [12755, 12756, 12757, 12758]
2023-04-25 : [12859, 12864, 12865, 12866, 12867, 12868, 12869, 12870, 12871, 12872, 12873, 12874]
```

Figure 6.1: List of the selected runs of LST-1 observations from 2023. The runs that refer to the night of April 25th 2023 are 12.

The evolution of significance and excess of the LST-1 dataset from 2023 are presented in Figure 6.2. The detection of a relatively strong signal is consistent with the predictions based on the periodicity observed by Fermi in the HE band [39], which anticipated a high-state of emission from the source in the current year.

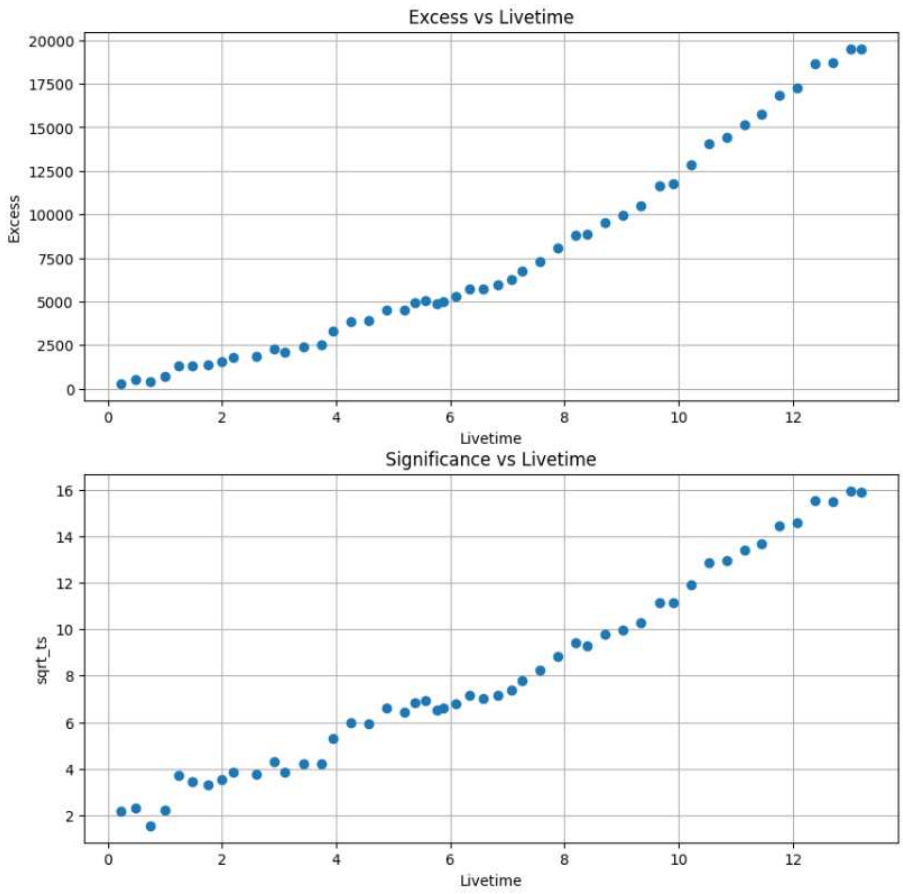

Figure 6.2: Evolution in time of excess (*top*) and significance (*bottom*) of LST-1 observations of PG 1553+113 from 2023.

The light curve of LST-1 observations of PG 1553+113 from 2023 is derived using a **night-wise** binning approach, covering data from a total of 11 nights (Fig.6.3). The light curve exhibits an upper limit which arises from the low detected significance in that specific bin (significance threshold of 2σ). The other data points are characterized by **error bars** with significantly different sizes. This disparity is due to the fact that the data points with smaller error bars correspond to nights of longer observation time. As a result, these nights yield a higher number of counts, leading to improved statistics and a more accurate error estimation.

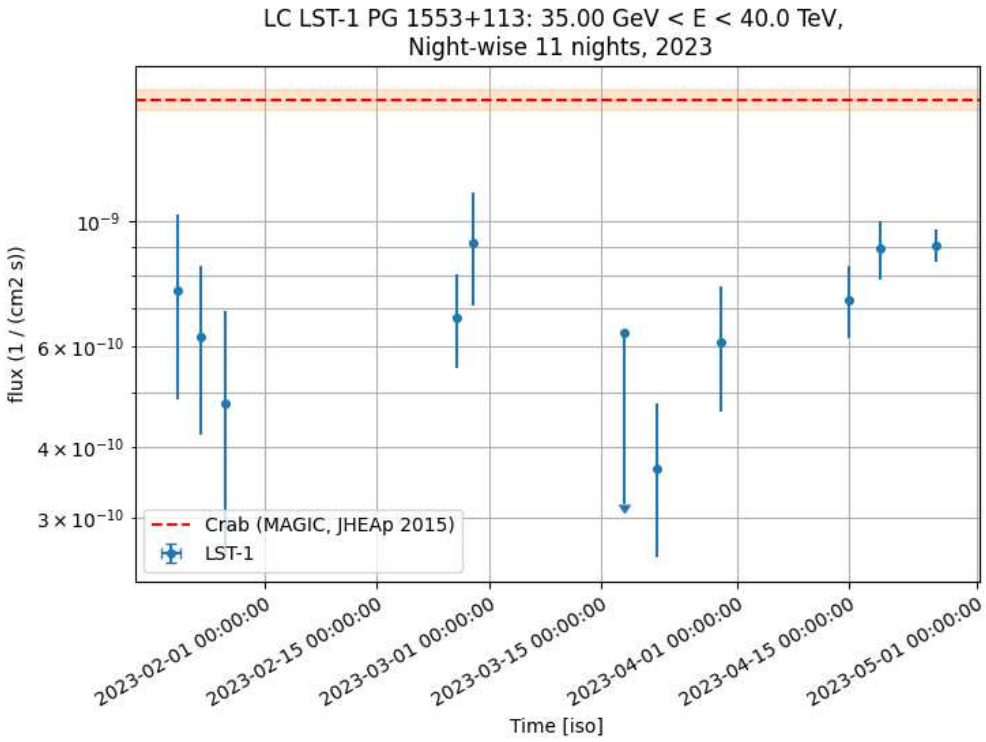

Figure 6.3: PG 1553+113 light curve of observations from 2023. It is obtained using a night-wise binning, including a total of 11 nights.

Among these nights, particular emphasis will be placed on the last one, April 25$^{\text{th}}$ 2023, as it offers the most extensive observation time (3.72 hours). These observations are of special interest since they allow the investigation of potential intra-night variability.
In the following sections, the outcomes derived from the analysis of this specific night will be presented.

6.2 Outcomes from single-night analysis

In this section are highlighted the results of the analysis of the night between April 25$^{\text{th}}$ and 26$^{\text{th}}$ 2023: the theta-squared distribution in Sec. 6.2.1, the spectral energy distribution in Sec. 6.2.2 and the light curve in Sec. 6.2.3.

6.2.1 Theta-squared distribution

The θ^2 distributions and excess plot are computed for the dataset including the 12 runs from the single night of observation. The θ^2 distribution is calculated for the **stacked dataset**, but also for **each run individually**. In this latter case, the total energy range from 10 GeV to 1 TeV is divided into four intervals, for a better investigation of the emission. The assumed

energy intervals are: 10 - 50 GeV, 50 - 300 GeV, 300 - 500 GeV, 500 GeV - 1 TeV. An example is shown in Figure 6.4, where is represented the θ^2 distribution for the Run 12869. The plots illustrate that the energy interval exhibiting the greatest significance is 50 - 300 GeV, reaching a value of 4.94σ. This implies a potentially significant detection of γ-ray emission from the source, as it closely approaches the 5σ threshold indicative of a relevant signal presence.

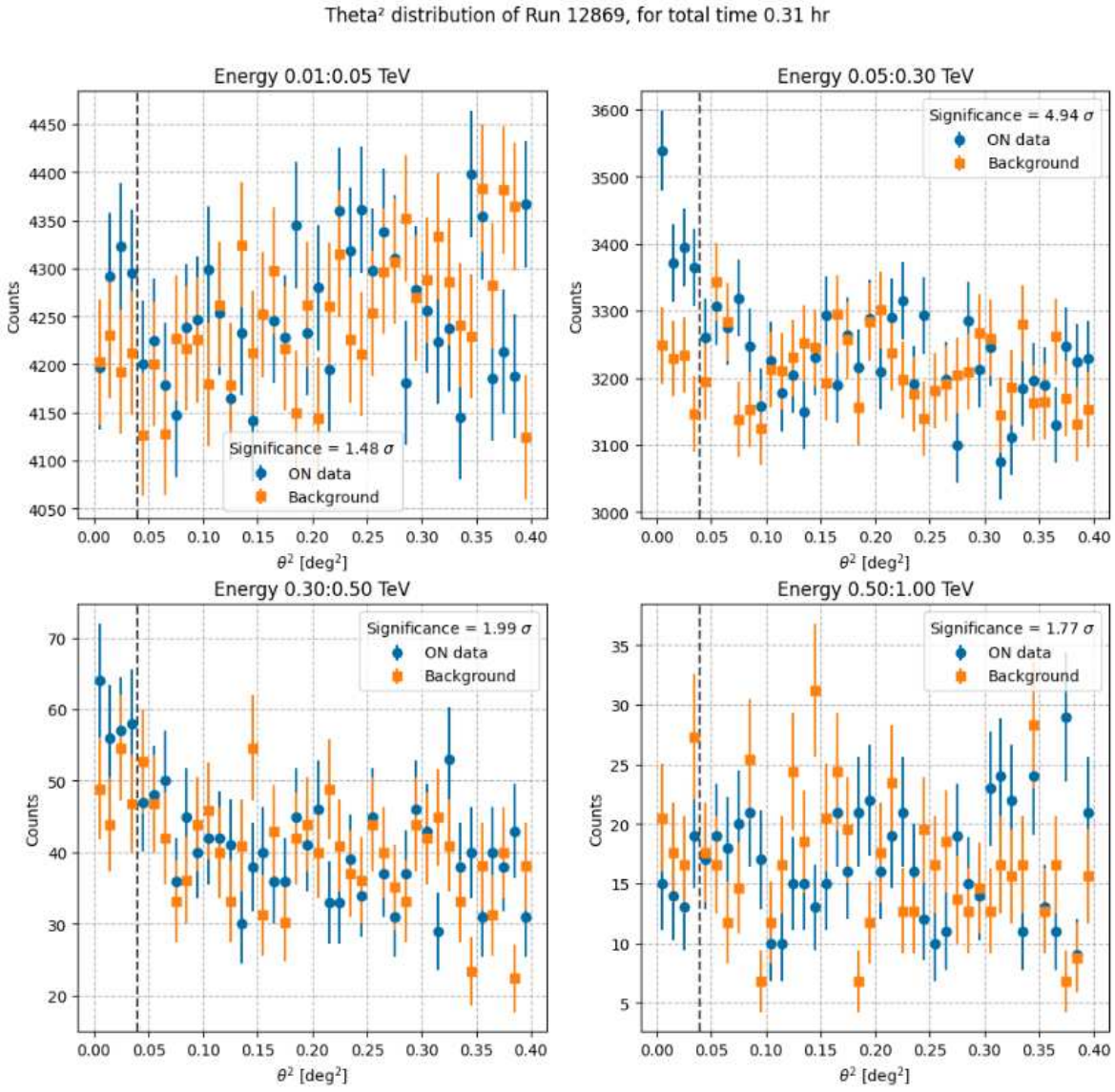

Figure 6.4: θ^2 distributions of Run 12869 for different energy intervals. The total observation time is of 0.31 hour. The highest significance is in the interval 50 - 300 GeV, with a value of 4.94σ.

Then, in Figure 6.5 is represented the θ^2 distribution of the stacked dataset, for which the **total significance** is equal to 12.55σ. This strongly indicates the **detection of a γ-ray signal** from the source. This is further demonstrated by the excess counts plot in Figure 6.6, where it

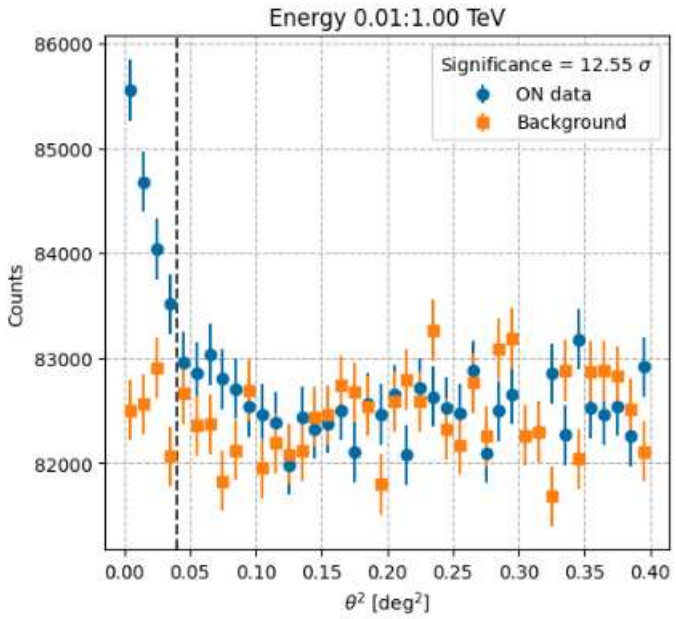

Figure 6.5: θ^2 distribution of the stacked dataset. The total significance is equal to 12.55σ.

becomes evident that the signal exceeds the background counts.

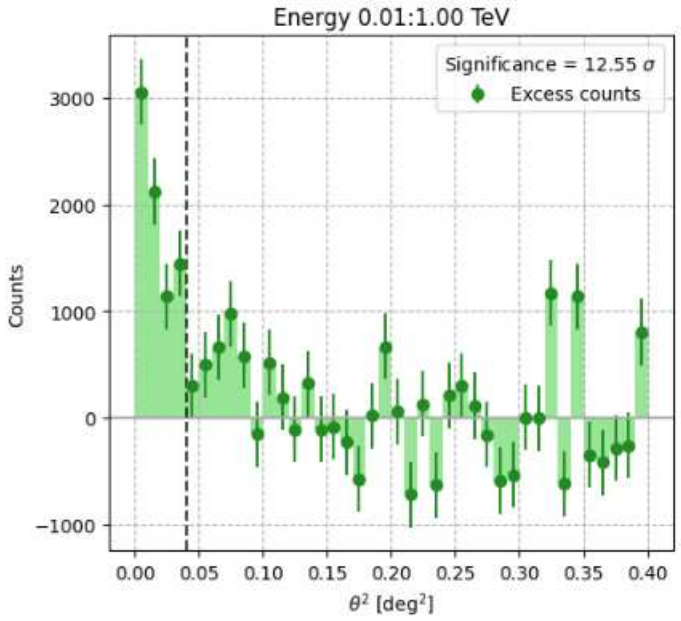

Figure 6.6: Excess counts computed for the stacked dataset. The signal clearly exceeds the background counts.

6.2.2 Spectrum and energy distribution

In Figure 6.7, the SED of PG 1553+113 from observations of the single night. It is calculated dividing the reconstructed energy range in 5 energy bins. LST-1 flux points range from ∼40 GeV to ∼400 GeV and they are fitted with a **Log Parabola spectral model** combined with an **EBL absorption spectral model**.

The **LogParabola** spectral model is described by the equation 6.2:

$$\Phi(E) = \Phi_0(\frac{E}{E_0})^{-\alpha-\beta log(\frac{E}{E_0})} \tag{6.2}$$

where $\Phi(E)$, Φ_0 and E_0 are the same quantities of the power-law model in Section 5.2.4, α describes the slope of the spectrum. β indicates the curvature: a positive value of β results in a concave spectrum, while a negative value results in a convex spectrum. The **EBL** spectral model (Dominguez) is the same as described in Section 5.2.4.

In the SED are represented both the observed and intrinsic flux points, corrected for the EBL absorption. The region in which points could be considered compatible with the measured data is represented in grey. The corresponding residuals are also shown.

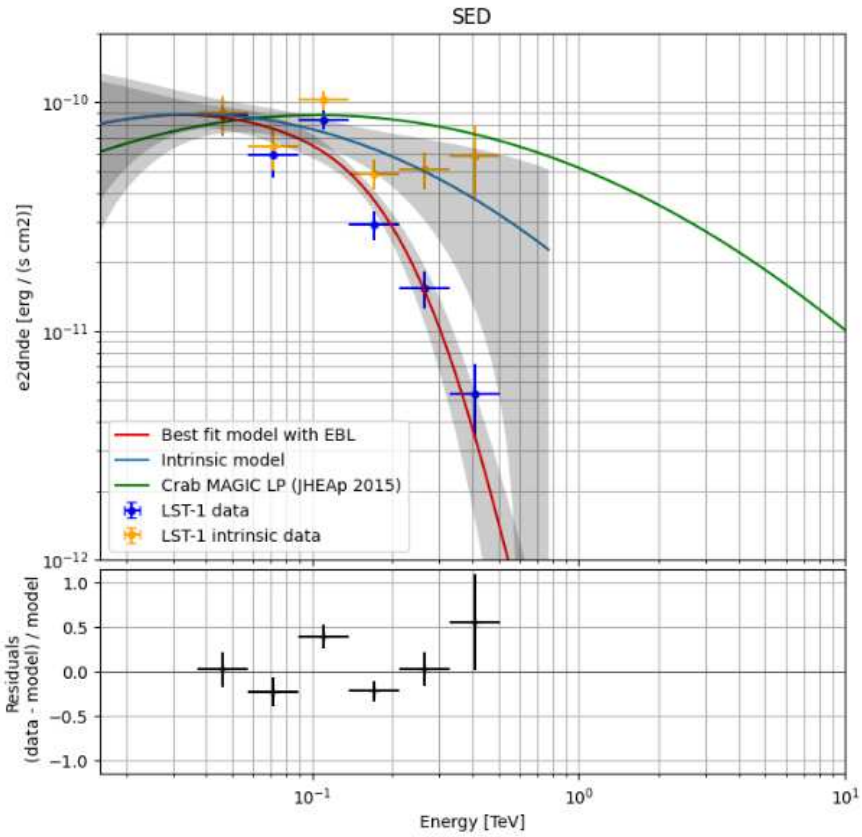

Figure 6.7: (*Top*) The PG 1553+113 SED calculated dividing the reconstructed energy range into 5 energy bins. The observed flux is represented by blue points and it is fitted with a Log Parabola + EBL. The intrinsic flux is represented by yellow points and fitted with the model without the EBL. The green line is the Crab reference. The grey region is the 'error' zone. (*Bottom*) SED residuals plot.

Then, the differential spectrum (observed and intrinsic) is computed and displayed in Figure 6.8.

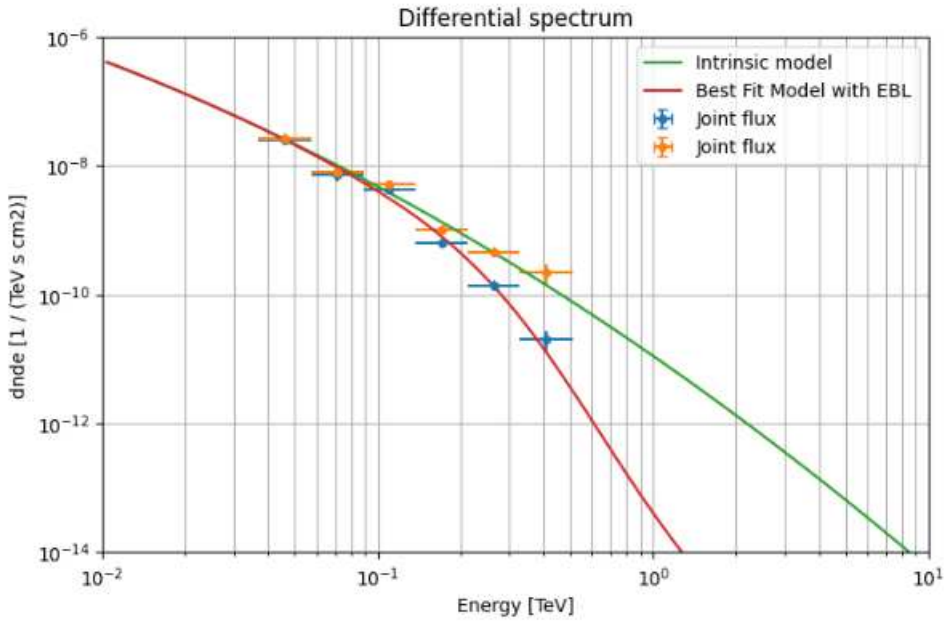

Figure 6.8: The observed (*blue*) and deabsorbed (*yellow*) differential spectrum of PG 1553+113 from observations taken on the single night.

Additionally, in Figure 6.9 is represented the **Test Statistic (TS) profile**, a graphical representation commonly used to explore the behavior of a parameter (usually the source flux or spectral index) as it deviates from a reference value. Here, the goodness of fit of the model parameters related to the SED ($E^2 \cdot dN/dE$) is evaluated, using the **fit statistic difference**, which mathematically is: TS(varied) - TS(reference). The fit statistic is a measure of how well a particular model fits the observed data. Observing a fit statistic difference of zero around each point in the TS profile, suggests that the parameter values are consistent with the reference value (often set to the best-fit value) within the uncertainties. This result does not necessarily mean that the reference model is the best or only valid model. It just indicates that the parameter values are *compatible* with the data points within their uncertainties.

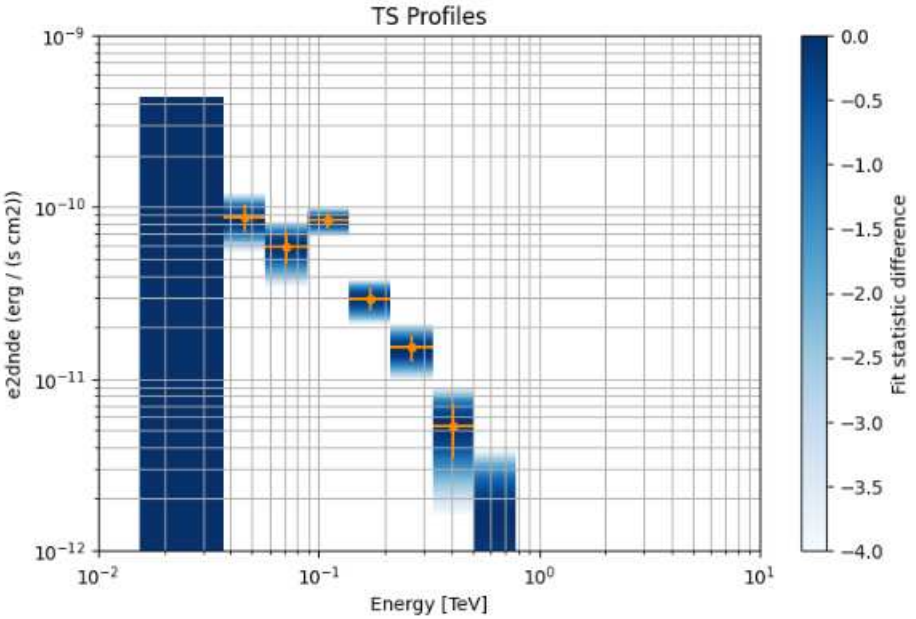

Figure 6.9: TS profile of the single night dataset.

Excess counts are presented in Figure 6.10, where are calculated the predicted and detected counts. The agreement is better at lower energies.

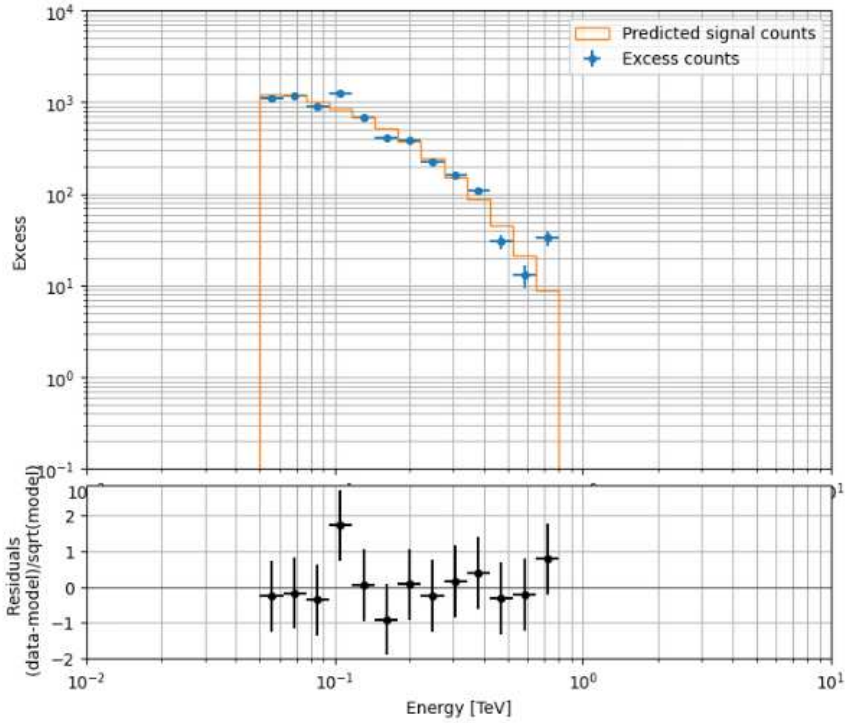

Figure 6.10: (*Top*) Predicted and detected counts of PG 1553+113. (*Bottom*) Residuals plot.

6.2.3 Light Curve

The light curve is computed considering a time binning of the order of minutes, to search for rapid changes in the flux. The total time interval for the selected runs covers 3.72 hours. In Figure 6.11 is presented the light curve obtained dividing the time interval in bins of **30 minutes**, finding a balance between having enough counts (therefore, enough significance) to compute each data point and a sufficient number of data points to facilitate variability analysis.

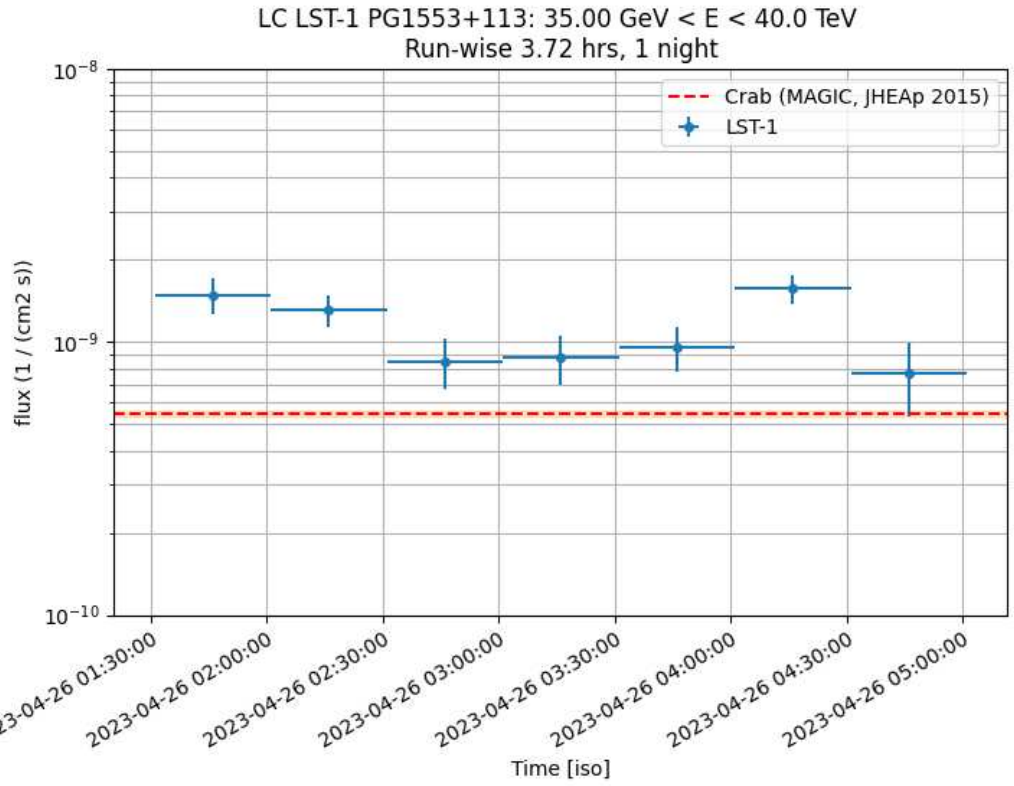

Figure 6.11: Light curve of PG 1553+113 of the night of April 25th 2023. It is computed using a time binning of 30 minutes.

This light curve is fitted with a **constant flux** (Fig. 6.12), to evaluate how much the flux emitted by PG 1553+113 during that specific night diverges from an unchanging behavior. The deviation from the constant flux can be quantified by the residuals, from which it is noticeable that data points exhibit substantial deviations from zero, indicating that a constant flux is an **inadequate** description of the emission.

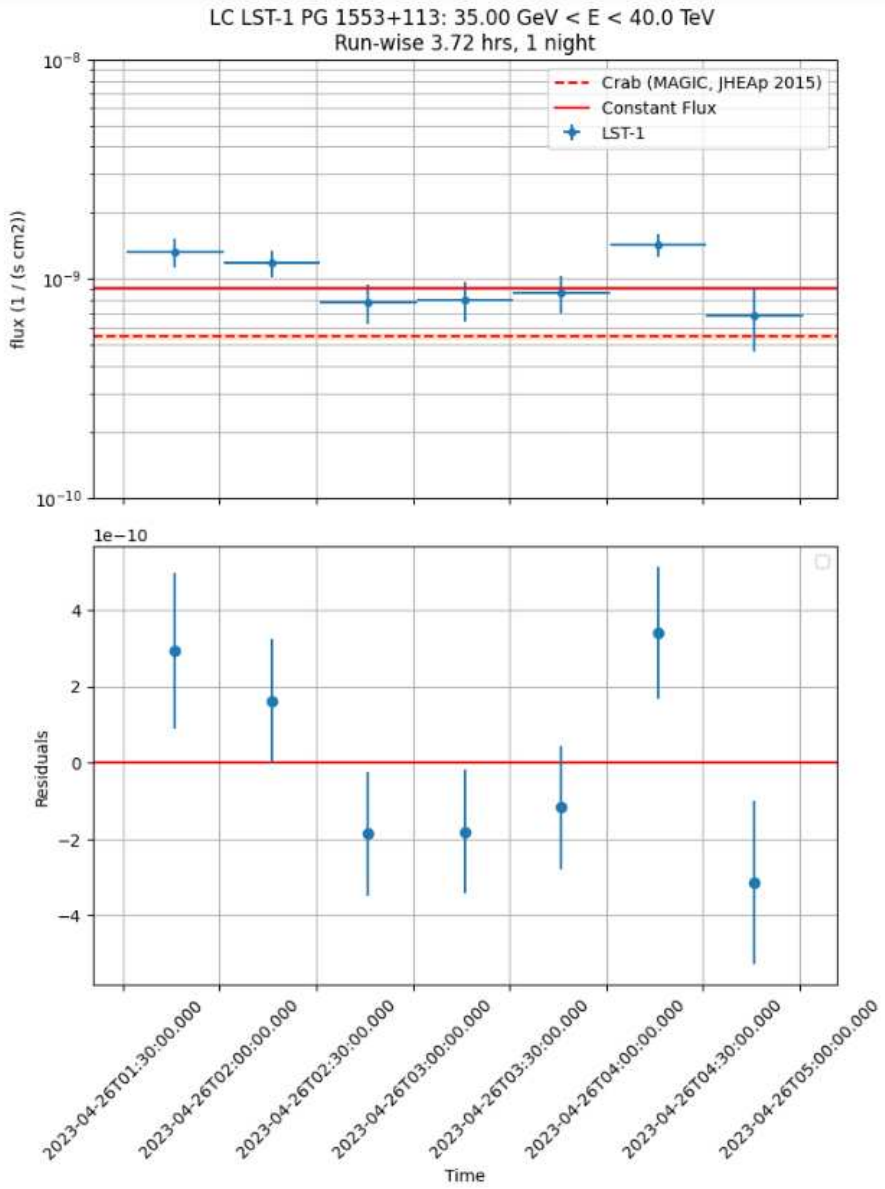

Figure 6.12: (*Top*) Flux points of the light curve are fitted with a constant flux. (*Bottom*) Residuals plot.

As in Section 5.3.2, a χ^2 test is performed, and the χ^2_{red} is calculated, using the same equations as before. They are found to be:

$$\begin{aligned} \chi^2 &= 17.06224149999541 \\ \chi^2_{red} &= 2.8437069166659015 \end{aligned} \tag{6.3}$$

The obtained χ^2_{red} value indicates that the flux emitted from PG 1553+113 during that specific night is **not consistent** with the hypothesis of constancy. This outcome **hints at the presence of intra-night variability in the VHE regime**, a remarkable result that has never been achieved before.

Chapter 7

Conclusions

In this thesis is presented the analysis of the extreme blazar PG 1553+113, performed using early data from LST-1. The original work of this thesis consists of performing the analysis *exclusively* utilizing data from LST-1, representing the **first time** such an approach has been undertaken in the High Energy group at the University of Padua.
This task involves approaching an instrument that is still in **commissioning phase**, making the entire process more complex.

Long-term monitoring

An important outcome of this analysis is the extensive **long-term monitoring of a blazar with LST-1**. The dataset containing observations from March 2021 to April 2023 of PG 1553+113, represents one of the longer time interval related to a blazar that has been analysed using data from LST-1. This monitoring period provides the opportunity to examine the dynamic behavior of a blazar over an extended timeframe, enabling the investigation of both short-term and long-term fluctuations in its emissions. *The flux collected by LST-1 from PG 1553+113 corresponds to a **variable emission**, in accordance with blazar's typical characteristic.* A high-state of emission of the source is detected in 2023, with a deep observation of a flare in April 2023.

Multi-wavelength characterization

The long-term monitoring enables a comprehensive **multi-wavelength characterization** of PG 1553+113, including data collected by LST-1. *The analysis performed in this thesis enables, for the **first time**, the **inclusion of LST data** in a multi-wavelength perspective.* This kind of work opens the possibility for future studies involving correlations across spectral bands, where the contribution of LST can be utilized for the first time. Furthermore, it will also facilitate investigations into the emission processes considered responsible for VHE emissions.

Analysis of flaring activity and intra-night variability

The April 25th 2023 flare represents the brightest state of PG 1553+113 during the expected high-state period in 2023. The extracted light curve is divided in small time binning to allow a better investigation of a potential short-term variability.

A remarkable result, deriving from the analysis of the flare, is that *from statistical analysis is found an* ***hint of intra-night variability***. This potential variability in the VHE regime is an outcome that has **never been achieved before**. The variability with this timescale is crucial to investigate compact structures responsible of the emission in the jet, the cooling process and the acceleration mechanisms. This unprecedented result requires further studies to achieve a deeper understanding of the phenomenon and to probe source emission.

Future prospects

PG 1553+113 has demonstrated notable variability and periodicity, that in addition to its status as a candidate binary system, make it an object of considerable scientific interest. A continuous monitoring will be necessary, to capture and understand PG 1553+113 behaviour expecially in the VHE band, that remains poorly known until the implementation of suitable instruments.

Considering the high tecnhological capabilities of LST-1 and in general of the CTA experiment, it is expected that significant results will be obtained in the near future. This will enables to investigate previously unexplored or poorly known regions of the VHE spectrum and further enhance the understanding of VHE astrophysical phenomena.

Acknowledgments

I would like express my gratitude to my supervisor, Mosè Mariotti, who introduced me to this complex and fascinating field, instilling in me the importance of continuous learning and staying informed to excel in one's work. I extend my thanks to my co-supervisor, Davide Miceli, who has been my guide and reference point throughout my journey, teaching me to work with precision and ambition. I thank the whole research group in Padua, Elisa Prandini and Ivana Batkovic, for their constant availability and support.

I thank my family, who allowed me to get this far and never stopped believing in me.
I thank the people closest to me, for their constant support that saved me many times.
I thank my little girl, without whom it would not have been the same.

With this, an important chapter in my life comes to a close, and I look forward to discovering what lies ahead.

Bibliography

[1] P. Padovani and D. M. Alexander et al. Active galactic nuclei: what's in a name? *The Astronomy and Astrophysics Review*, 25(1), aug 2017.

[2] Volker Beckmann and Chris R. Shrader. The agn phenomenon: open issues, 2013.

[3] Elisa Prandini and Gabriele Ghisellini. The blazar sequence and its physical understanding. *Galaxies*, 10(1):35, feb 2022.

[4] Krishna K. Singh and Peter J. Meintjes. Characterization of variability in blazar light curves. *Astronomische Nachrichten*, 341(713):713–725, July 2020.

[5] Mansutti De Angelis and Persic. Very-high energy gamma astrophysics. *Rivista del Nuovo Cimento*, 31, 12 2007.

[6] Jun-Hui Fan and Yong et al. Huang. Radio variability and relativistic beaming effect for blazars. *Publications of the Astronomical Society of Japan*, 61(4):639–643, 2009.

[7] G. Ghisellini and F. Tavecchio. The blazar sequence: a new perspective. *Monthly Notices of the Royal Astronomical Society*, 387(4):1669–1680, jul 2008.

[8] G. Fossati, L. Maraschi, A. Celotti, A. Comastri, and G. Ghisellini. A unifying view of the spectral energy distributions of blazars. , 299(2):433–448, September 1998.

[9] D. Donato, G. Ghisellini, G. Tagliaferri, and G. Fossati. Hard x-ray properties of blazars. *Astronomy &amp Astrophysics*, 375(3):739–751, sep 2001.

[10] G. Ghisellini, A. Celotti, G. Fossati, L. Maraschi, and A. Comastri. A theoretical unifying scheme for gamma-ray bright blazars. , 301(2):451–468, December 1998.

[11] G. Ghisellini, C. Righi, L. Costamante, and F. Tavecchio. The fermi blazar sequence. *Monthly Notices of the Royal Astronomical Society*, 469(1):255–266, apr 2017.

[12] J. R. Primack and A. Dominguez et al. Extragalactic background light and gamma-ray attenuation. In *AIP Conference Proceedings*. AIP, 2011.

[13] Alberto Franceschini. Photon-Photon Interactions and the Opacity of the Universe in Gamma Rays. *Universe*, 7(5):146, May 2021.

[14] Alberto Franceschini and Giulia Rodighiero. The extragalactic background light revisited and the cosmic photon-photon opacity. , 603:A34, July 2017.

[15] J. Dorigo Jones and S. D. et al. Johnson. Improving blazar redshift constraints with the edge of the Ly α forest: 1ES 1553+113 and implications for observations of the WHIM. , 509(3):4330–4343, January 2022.

[16] MAGIC Collaboration and MWL partners. *The variability patterns of the TeV blazar PG 1553+113 from a decade of MAGIC and multi-band observations*. submitted to MNRAS (2023).

[17] M. Tavani, A. Cavaliere, P. Munar-Adrover, and A. Argan. The blazar PG 1553113 as a binary system of supermassive black holes. *The Astrophysical Journal*, 854(1):11, feb 2018.

[18] W. Heitler. Quantum theory of radiation. 1954.

[19] *Cherenkov radiation - an overview*. ScienceDirect Topics.

[20] *https://www.cta-observatory.org/*.

[21] D. Bose and V. R. Chitnis et al. Ground-based gamma-ray astronomy: history and development of techniques. *The European Physical Journal Special Topics*, 231(1):3–26, dec 2021.

[22] Jürgen Knödlseder. The cherenkov telescope array, 2020.

[23] *https://www.cta-observatory.org/ctao-releases-layouts-for-alpha-configuration/*. 2022.

[24] G. Maier, L. Arrabito, K. Bernlöhr, J. Bregeon, P. Cumani, T. Hassan, J. Hinton, and A. Moralejo. Performance of the cherenkov telescope array, 2019.

[25] *Science with the Cherenkov Telescope Array*. WORLD SCIENTIFIC, feb 2018.

[26] https://www.cta-observatory.org/lst-prototype-records-its-first light/.

[27] H. Abe, A. Aguasca, and I. et al. Agudo. Status and results of the prototype lst of cta. page 872, 07 2021.

[28] Abelardo Moralejo. Lst-1, the large-sized telescope prototype of cta. status and first observations. *17th International Conference on Topics in Astroparticle and Underground Physics*, 2021.

[29] Maria Isabel Bernardos Franca Cassol Luca Foffano et al. Rubén López-Coto, Andrés Baquero. lstchain: An analysis pipeline for lst-1, the first prototype large-sized telescope of cta. *30th Astronomical Data Analysis Software and Systems*, page 357, Nov 2020.

[30] R. López-Coto, A. Moralejo, and M. Artero et al. Physics performance of the large-sized telescope prototype of the cherenkov telescope array, 2021.

[31] LST Analysis school. January 2022.

[32] D. Berge, S. Funk, and J. Hinton. Background modelling in very-high-energy i/i-rayastronomy. *Astronomy &amp Astrophysics*, 466(3):1219–1229, apr 2007.

[33] A. M. Hillas. Cerenkov Light Images of EAS Produced by Primary Gamma Rays and by Nuclei. In *19th International Cosmic Ray Conference (ICRC19), Volume 3*, volume 3 of *International Cosmic Ray Conference*, page 445, August 1985.

[34] Mathieu de Naurois. Analysis methods for atmospheric cerenkov telescopes. 08 2006.

[35] John E. Ward, Javier Rico, and Tarek Hassan. The instrument response function format for the cherenkov telescope array, 2015.

[36] J. S. Perkins. Blazar discoveries with veritas, 2009.

[37] S. Gillessen and H. L. Harney. Significance in gamma-ray astronomy – the li &amp ma problem in bayesian statistics. *Astronomy &amp Astrophysics*, 430(1):355–362, jan 2005.

[38] C. Deil A. Donath and R. Terrier et al. Gammapy: v.0.19. November 2021.

[39] M. Ackermann and Ajello et al. Multiwavelength Evidence for Quasi-periodic Modulation in the Gamma-Ray Blazar PG 1553+113. , 813(2):L41, November 2015.

[40] Vinit Dhiman et al. Multiband variability of the TeV blazar PG 1553113 with iXMM–newton/i. *Monthly Notices of the Royal Astronomical Society*, 506(1):1198–1208, jun 2021.

[41] Krishna K. Singh and Peter J. Meintjes. Characterization of variability in blazar light curves. *Astronomische Nachrichten*, 341(713):713–725, July 2020.